Electronic Supplementary Material (ESI) for Energy & Environmental Science.

Supplemental information

MOF Nanosheets as Ion Carriers for Self-Optimized Zinc Anode

Hanmiao Yang, Kaiyue Zhu, Weili Xie, Liming Zhang, Weikang Jiang, Weijian Li, Zhengsen Wang, Weishen Yang

This PDF file includes:

Figure S1 to S35
References
Captions for Movie S1

Other Supplementary Materials for this manuscript include the following:

Movie S1
Table S1

Electrolyte preparation of $ZnSO_4$ and $ZnSO_4$ with dynamic metal organic framework (MOF) nanosheets.

The 0.1~2 M $ZnSO_4$ electrolytes were prepared by dissolving certain amounts of $ZnSO_4 \cdot 7H_2O$ in ultrapure water according to the molality (M, mol L^{-1}). Dynamic MOF nanosheets (DMNs) regulated electrolyte was prepared by adding trace amounts of $CuSO_4 \cdot 5H_2O$ and trimesic acid solution into 0.1~2 M $ZnSO_4$ solution. Certain trimesic acid was dissolved in ethanol, and the volume ratio of ethanol to water in the final electrolyte is 1:5. Finally, the concentrations of $CuSO_4$ and trimesic acid were 0.002 M and 0.005 M, respectively. The trace amounts of Cu^{2+} will be replaced by zinc anode and slightly adjust the pH of electrolyte thereby promoting the generation of DMN by deprotonating H_3BTC. The as-replaced zinc anode will be covered by (002)-oriented zinc deposit soon together with the extinction of hydrogen evolution reaction (HER) from Cu. This fomulation is applicable to coin cells with limited electrolyte and need to be adjusted in rich-electrolyte system. When adopting 2 M $ZnSO_4$ electrolyte with DMNs, addition of $CuSO_4$ is not necessary as HER in highly concentrated $ZnSO_4$ is enough for deprotonating H_3BTC. Note that in the full cell with the MnO_2 cathode, $MnSO_4$ (0.2 M) was additionally introduced to the DMN-regulated electrolyte.

Separation of Zn-MOF powders

Significantly, the concentration of DMNs in $ZnSO_4$ electrolytes appears to be insufficient for effective collection. In order to expedite the generation of Zn-MOF nanosheets, a novel approach was employed. A zinc foil decorated with Cu nanoparticles, was submerged in $ZnSO_4$ electrolytes containing ligands, facilitating the deprotonation of H_3BTC. Following a 24-hour immersion in 20 mL of 2 M $ZnSO_4$ electrolytes with ligands, a considerable amount of Zn-MOF nanosheets excessively propagated and aggregated, forming a precipitate. The precipitate was carefully gathered and subjected to thorough washing using deionized water and ethanol. Finally, it was dried at 60 °C for 12 hours to obtain the desired Zn-MOF nanosheets in a modified and improved manner.

Preparation of Zn-MOF-1 layer coated Zn foil.

Zn-MOF-1 layer coated zinc foil (Zn@Zn-MOF-1) was prepared by soaking zinc foil in the following solution 1 of 20 mL for 48 hours. Solution 1: the 0.5 M $ZnSO_4$ electrolyte with DMNs whose preparation process was stated aboved.

Preparation of Zn-MOF-2 layer coated Zn foil.

Zn-MOF-2 layer coated zinc foil (Zn@Zn-MOF-2) was prepared by soaking zinc foil in the following solution 2 of 20 mL for 48 hours. Solution 2: five times dilution of solution 1.

Preparation of Zn-MOF layer coated Cu foil.

Zn-MOF (including Zn-MOF-1 and Zn-MOF-2) layer coated Cu foil (Cu@Zn-MOF) was prepared by soaking zinc coated Cu foil (Zn deposition at 100 mA/cm^2 on Cu for 10 minute) in the following solution 3 of 20 mL for 48 hours. Solution 3: 3 times dilution of Solution 1.

Synthesis of MnO_2 nanorods.

β-MnO_2 was synthesized through a conventional hydrothermal method.[1] In a typical procedure, 30 mL of 0.1 M $KMnO_4$ solution was mixed with 30 mL of 0.6 M $MnSO_4$ solution. After stirring for 30 minutes, the above mixture was subsequently loaded into a stainless-steel autoclave with a Teflon liner and held at 140 °C for 12 h. After the reaction, the precipitate was collected and thoroughly washed with deionized water and ethanol, and finally dried in vacuum at 60 °C for 12 h.

Synthesis of $(NH_4)_2V_{10}O_{25}\cdot 8H_2O$ nanobelts.

$(NH_4)_2V_{10}O_{25}\cdot 8H_2O$ (NVO) was prepared via a hydrothermal method.[2] In a typical run, certain amounts of NH_4VO_3 (0.585 g) and $H_2C_2O_4$ (0.63 g) were added into deionized (DI) water under vigorous stirring for 30 minutes. Then the mixture was subsequently loaded into a stainless-steel autoclave with a Teflon liner and held at 130 °C for 12 h. After the reaction, the precipitate was collected and thoroughly washed with deionized water and ethanol and dried under vacuum at 60 °C for 12 h.

Preparation of cathodes.

To prepare a cathode, 60 wt% as-synthesized NVO or MnO_2 powders, 26 wt% Super-P, and 14 wt% polyvinylidene fluoride (PVDF) were mixed thoroughly and dispersed in N-methyl pyrrolidone (NMP). The resultant slurry was then uniformly coated onto 14 mm diameter stainless steel meshes (SSM) with an active mass loading of ~ 1 mg cm^{-2}, followed by vacuum drying at 100 °C for approximately 12 h.

Electrochemical measurements.

All electrochemical measurements were carried out at room temperature. Commercial zinc foil with a diameter of 14 mm and a thickness of 200 μm were purchased from Suzhou Sinero Technology Co., Ltd. CR2032-type coin cells were assembled to evaluate the electrochemical performances on a LAND battery test system. Glass fiber (GF/A, Whatman) was used as a separator in coin cells to separate the anode and the cathode. Electrochemical impedance spectroscopy (EIS) was measured on a Princeton PARSTAT electrochemical working station over the frequency rang from 0.01 to 100 kHz with a perturbation amplitude of 5 mV. Cyclic voltammetry and chronoamperometric measurements were conducted on a Princeton PARSTAT electrochemical working station.

Materials characterizations.

X-ray diffraction (XRD) was performed on an X'pert Pro-1 X-ray diffractometer with a Cu Kα1 X-ray source (λ = 1.5405 Å) to determine the phase structures. The data were recorded from 5º to 80º with an interval of 0.02º and a scan speed of 5º min^{-1}. The pole figures on the (002) crystal plane of zinc were measured by a SmartLab X-ray diffractometer. The morphologies of the samples were captured with a scanning electron microscopy (SEM, Quanta 200F). Microscopic morphologies and elemental mapping were obtained by field-emission scanning electron microscopy (FESEM, JSM-7900F) with a Max80 energy dispersive spectroscopy (EDS). The crystalline structures and morphologies of the samples were also acquired with transmission electron microscopy (TEM, HT7700) and high-resolution transmission electron microscopy (HRTEM, Titan Themis ETEM G3). The thickness and surface roughness of the samples were

analyzed by atomic force microscopy (AFM, JPK NanoWizard). The zeta potentials and dynamic light scattering results were acquired by a Nano laser particle size analyzer (Zetasizer Nano). The structures of dispersed MOFs were measured by a small angle X-ray scatterometer (SAXS, Saxes M2). The contact angels of the samples were measured by a drop shape analyzer (DSA100).

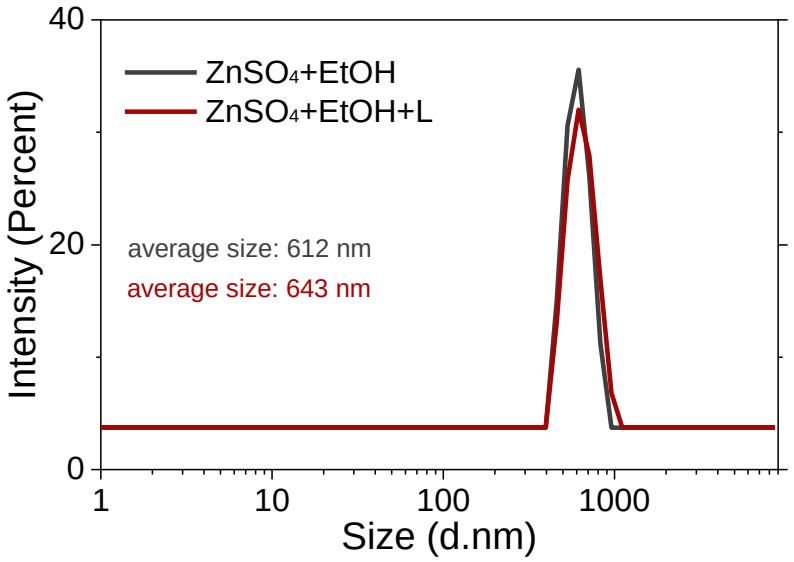

Figure S1. Dynamic light scattering (DLS) results of 0.1 M $ZnSO_4$ electrolytes in water-ethanol solvent mixture (EtOH: 20%, v/v) containing ligand or not.

The average size of the dispersed ethanol without ligand is 612 nm, while that with ligand is 643 nm. The slightly soluble ligand H_3BTC in water is concentrated in ethanol phase, and has a negligible influence on the size distribution of ethanol droplets.

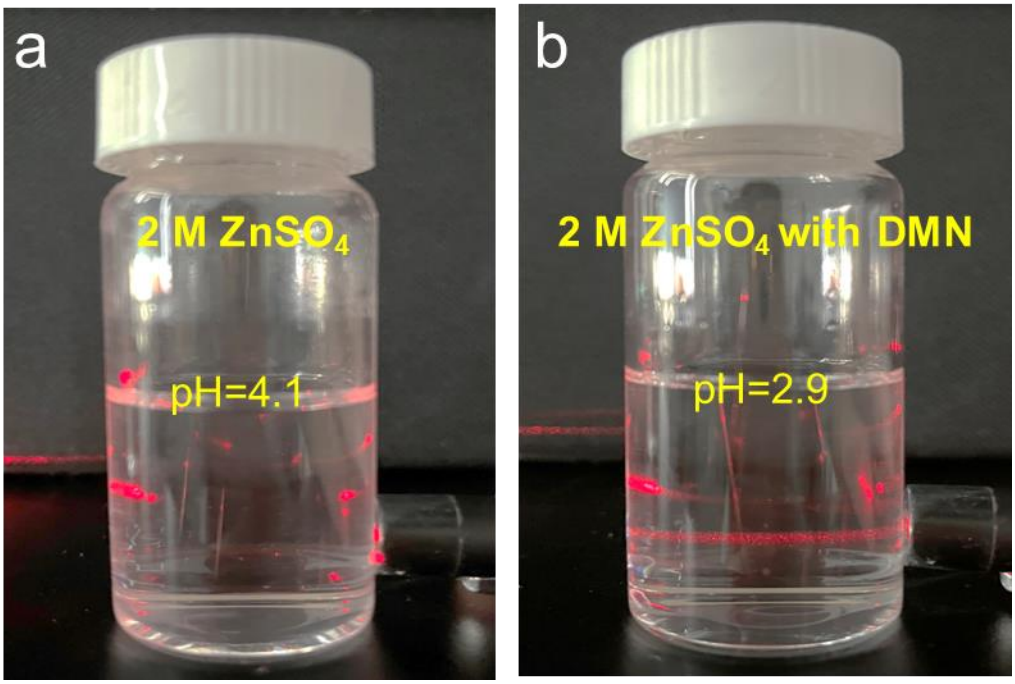

Figure S2. Optical photographs of (a) 2 M $ZnSO_4$ electrolyte, (b) 2 M $ZnSO_4$ electrolyte with DMNs.

In the absence of DMNs, the pure $ZnSO_4$ electrolyte does not exhibit the Tyndall phenomenon. However, after introducing ligands into the 2 M $ZnSO_4$ electrolyte, the solution remains colorless and transparent, yet displays a Tyndall light scattering effect, suggesting the presence of nano-scale particles within the solution.

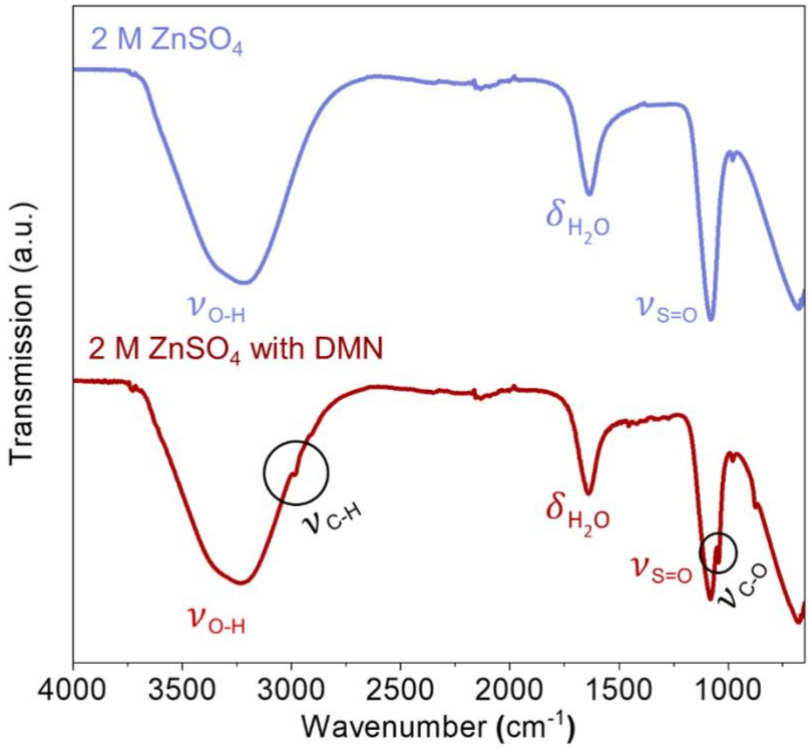

Figure S3. The Fourier-transform infrared spectra of 2 M $ZnSO_4$ and 2 M $ZnSO_4$ with DMNs.

The FTIR analysis demonstrates minimal disparity between 2 M $ZnSO_4$ and 2 M $ZnSO_4$ with DMNs in terms of their infrared signals. The weak absorbance bands observed at 2980 cm^{-1} and 1043 cm^{-1} regions, corresponding to C-H stretching and C-O stretching vibrations, respectively, are attributed to the presence of ethanol in the solution. However, despite the inclusion of ethanol, it appears to have little impact on the solvation structure of the electrolyte. Furthermore, the similar FTIR spectra in 2 M $ZnSO_4$ and 2 M $ZnSO_4$ with DMNs also suggests that there is a little amount of MOF nanosheets in the electrolyte, and the solvation structure remains largely similar in both the $ZnSO_4$ electrolyte with and without DMNs.

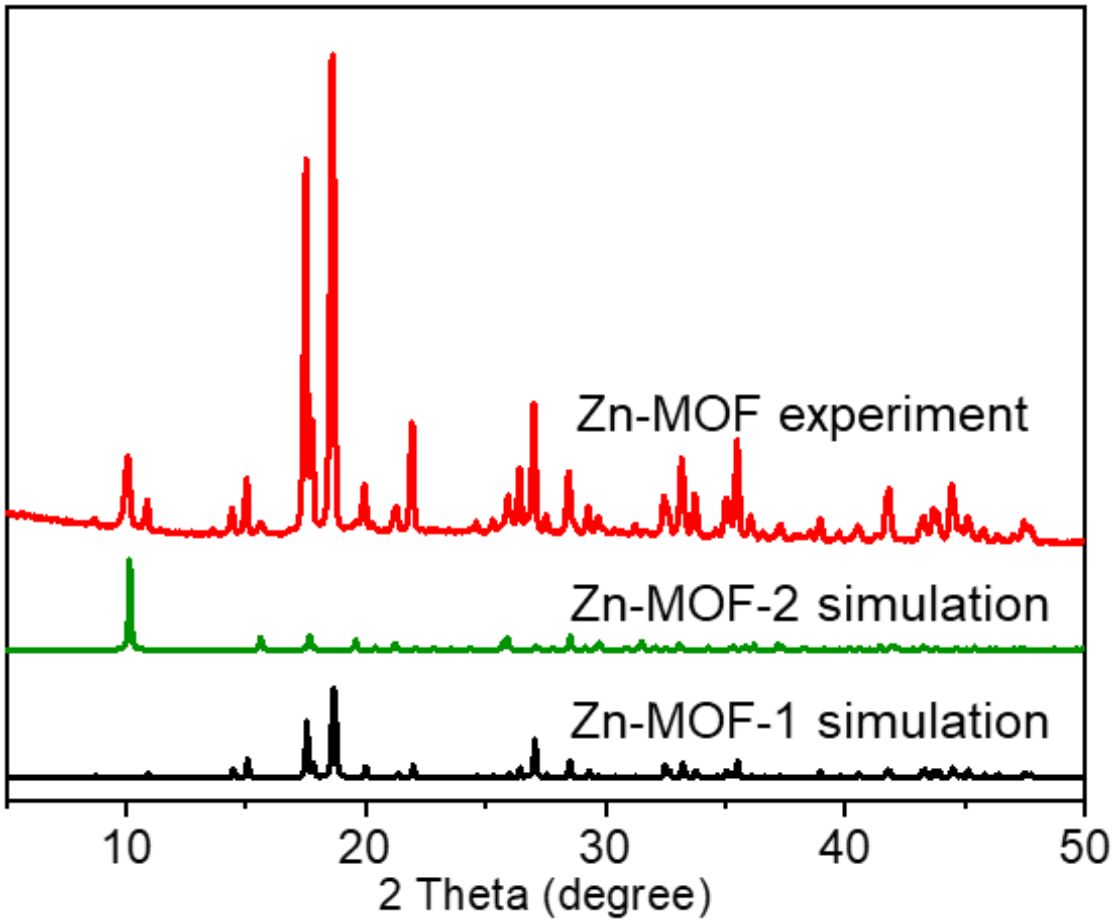

Figure S4. Powder XRD patterns of experimental Zn-MOF nanosheets (denoted as Zn-MOF experiment) appearing in the electrolyte solution and simulated based on the single-crystal data Zn-MOF-1 (CCDC-262703)[3] and Zn-MOF-2 (CCDC-823406)[4]. The method for powder separation from the electrolyte was stated in the Method Section.

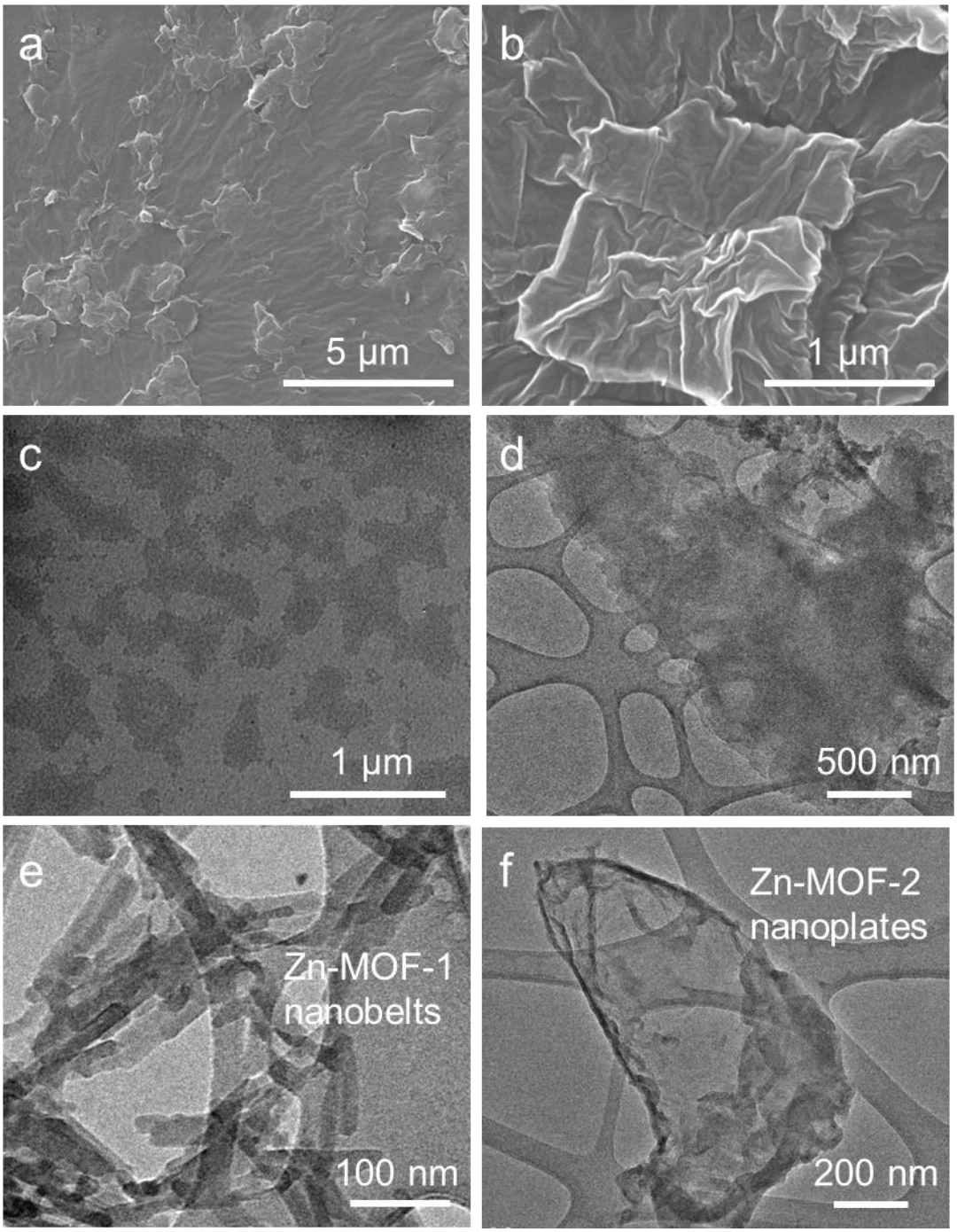

Figure S5. (a, b) SEM images with different magnifications and (c-f) TEM images of the flocculus (including nanobelts and nanoplates) appearing in the $ZnSO_4$ electrolyte with H_3BTC.

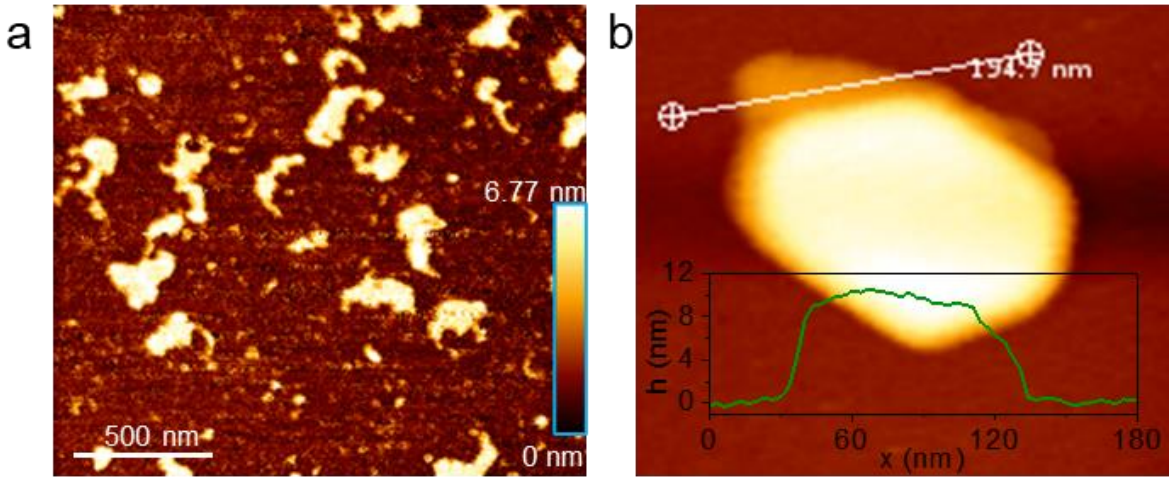

Figure S6. Atomic force microscopy (AFM) images of the dynamic MOF nanosheets appearing in the $ZnSO_4$ electrolyte with H_3BTC on the substrate of mica slice. The inset in (b) shows the height (h) profile of the nanosheets along the white line.

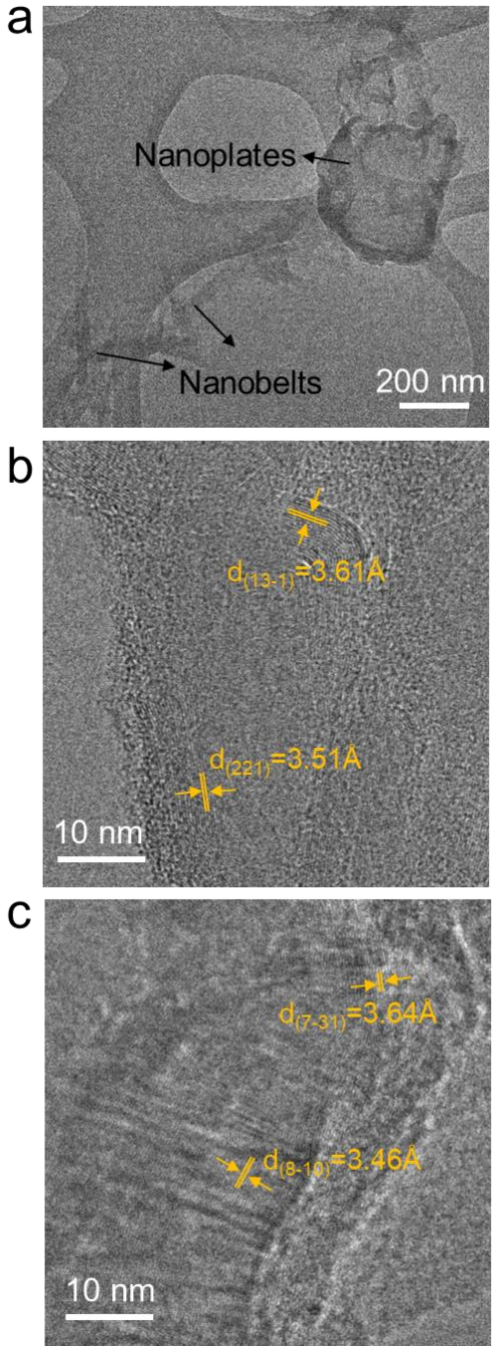

Figure S7. (a) TEM images of Zn-MOF nanosheets including Zn-MOF-1 nanobelts and Zn-MOF-2 nanoplates. High-resolution TEM images for (b) Zn-MOF-1 (CCDC-262703) nanobelts and (c) Zn-MOF-2 (CCDC-823406) nanoplates generated in the $ZnSO_4$ electrolyte with H_3BTC. The lattice spacings of 3.51 and 3.61 Å in (b) correspond well with the (221) and (13-1) planes of Zn-MOF-1 (CCDC-262703), while the lattice spacings of 3.46 and 3.64 Å in (c) are assigned to the (8-10) and (7-31) planes of Zn-MOF-2 (CCDC-823406).

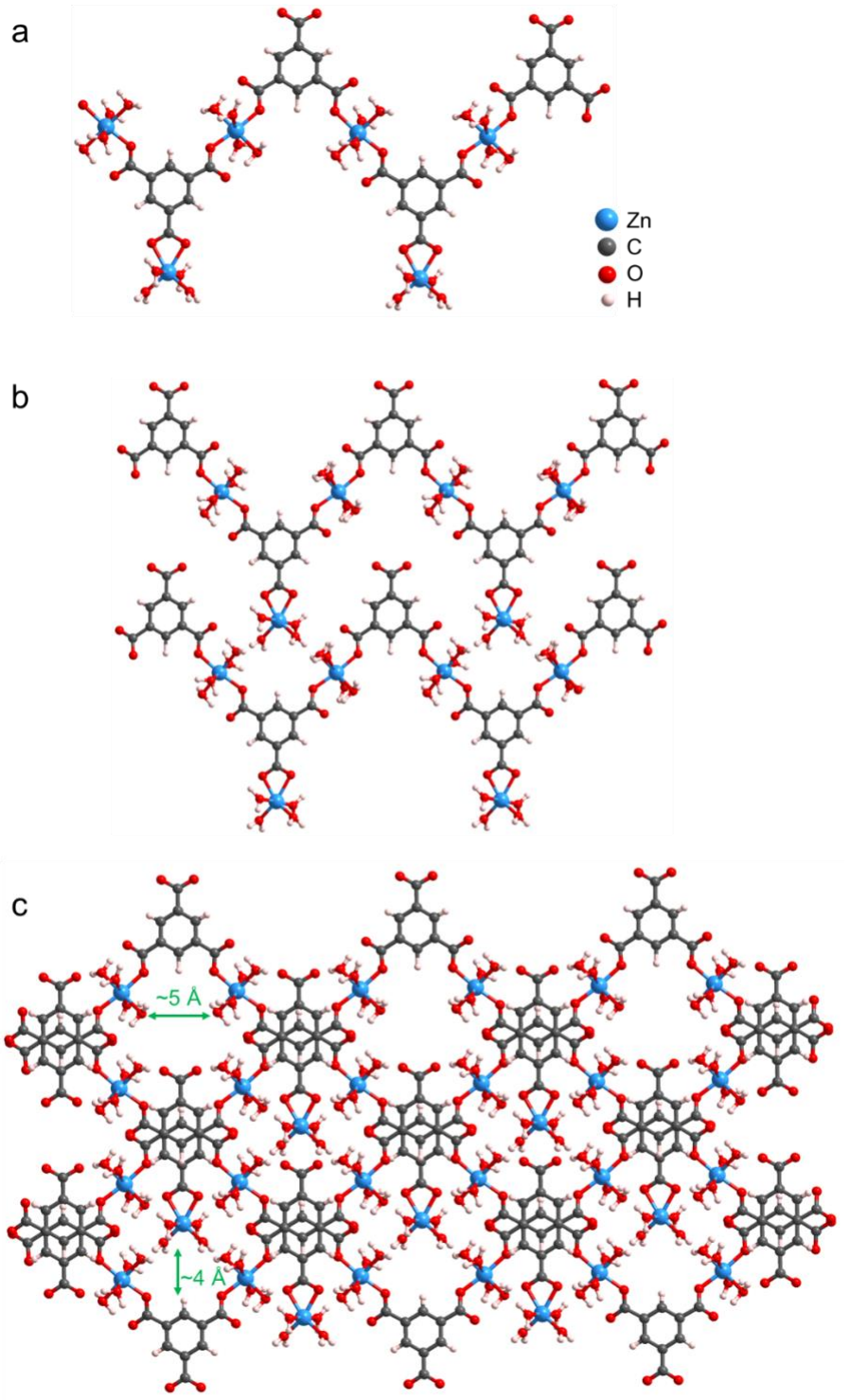

Figure S8. The crystal structures of Zn-MOF-1 (CCDC-262703). (a) One-dimensional (1D) chain structure; (b) two-dimensional (2D) layer structure consisting of 1D chains via hydrogen bonds (hydrogen bonds are omitted for clarity); (c) three-dimensional (3D) networks with pores (diameters of ~4 Å and ~5 Å) stacked by 2D layers through the π···π stacking interactions from benzene rings and O···H···O strong hydrogen bonds.

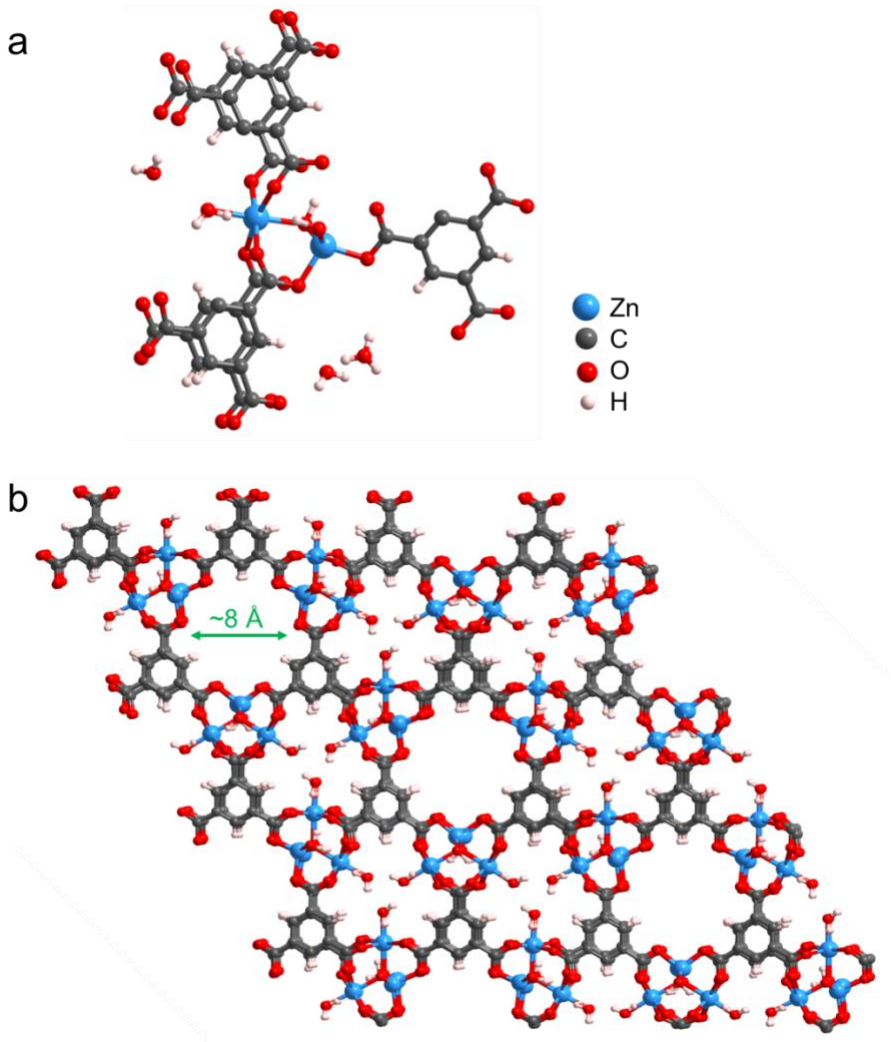

Figure S9. The crystal structures of Zn-MOF-2 (CCDC-823406). (a) The coordination environments around the center Zn; (b) 3D structures with pores (diameters of ~8 Å).

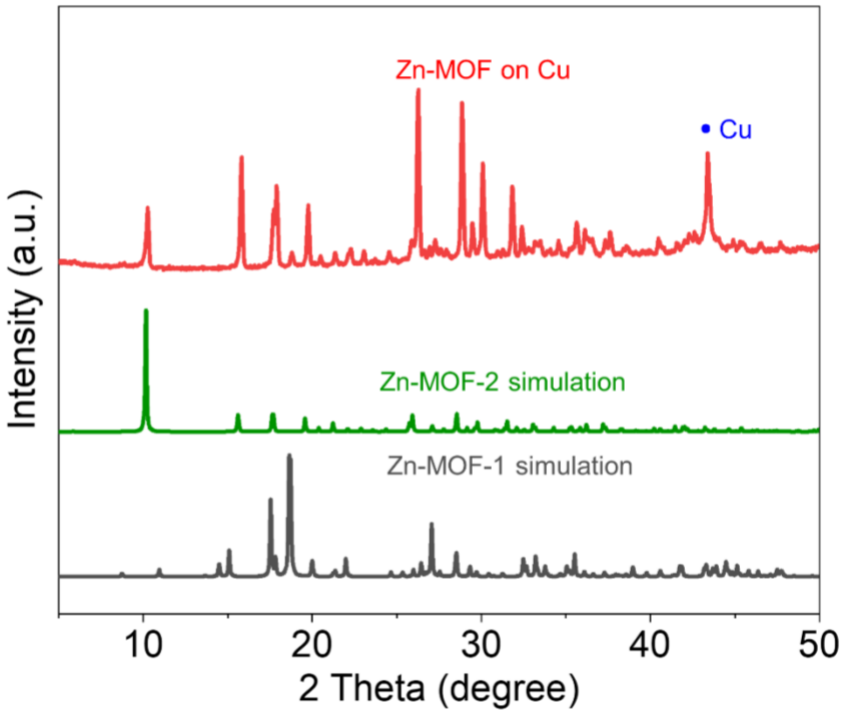

Figure S10. XRD pattern of Cu foil coated by Zn-MOF-1 and Zn-MOF-2 static films. The preparation process is stated in the previous method section

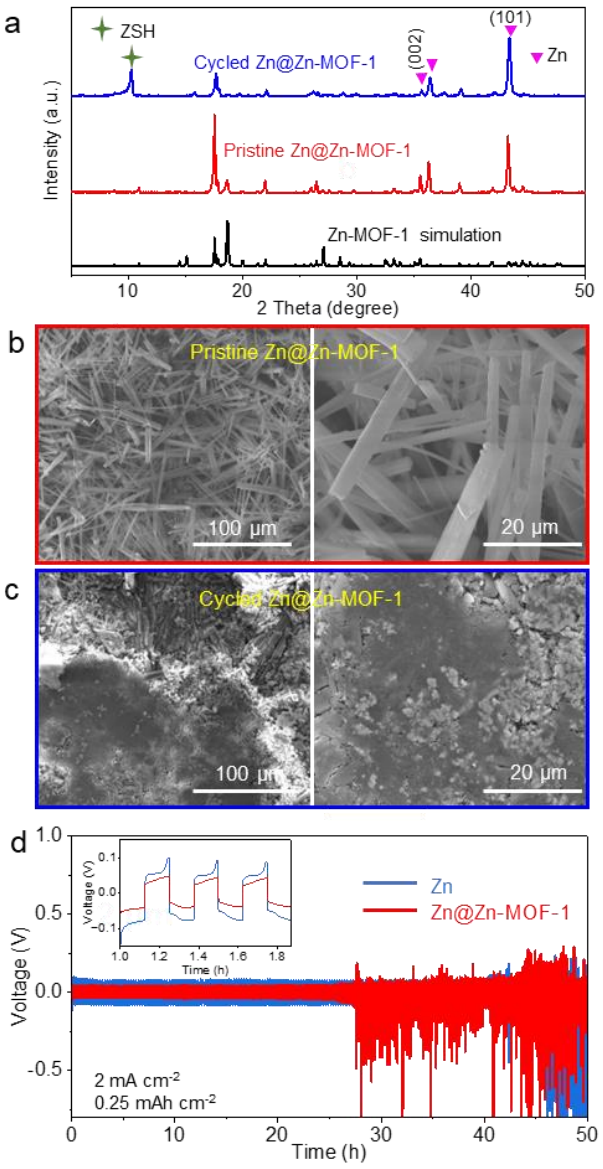

Figure S11. (a) The XRD patterns of zinc foil coated with the Zn-MOF-1 layer (denoted as Zn@Zn-MOF-1) and Zn@Zn-MOF-1 after cycling in $ZnSO_4$. The as-grown Zn-MOF-1 on zinc was well indexed to the standard simulation of Zn-MOF-1. SEM images of (b) pristine Zn@Zn-MOF-1 and (c) Zn@Zn-MOF-1 after cycling in $ZnSO_4$ for 50 hours. (d) Cycle performance of Zn||Zn and Zn@Zn-MOF-1||Zn@Zn-MOF-1 symmetric cells in pure $ZnSO_4$. The inset in (d) compares the detailed voltage profiles for bare Zn foil and Zn@Zn-MOF-1 in $ZnSO_4$ electrolyte.

Compared to pristine Zn@Zn-MOF-1, a large amount of byproduct $Zn_4(OH)_6SO_4 \cdot 3H_2O$ (ZSH, JCPDS No. 39-0689) is formed and the XRD intensity ratio of Zn (002) and Zn (101) is decreased for Zn@Zn-MOF-1 after cycling in $ZnSO_4$. In addition, the content of Zn-MOF-1 in Zn@Zn-MOF-1 after cycling in $ZnSO_4$ for 50 hours is lower than that in pristine Zn@Zn-MOF-1, indicating the instability of Zn-MOF-1. This is probably because Zn-MOF-1 undergoes a reduction reaction during Zn plating (see evidence in Figure 2c). Moreover, the as-deposited Zn covering the surface of the Zn-MOF-1 layers is irregular.

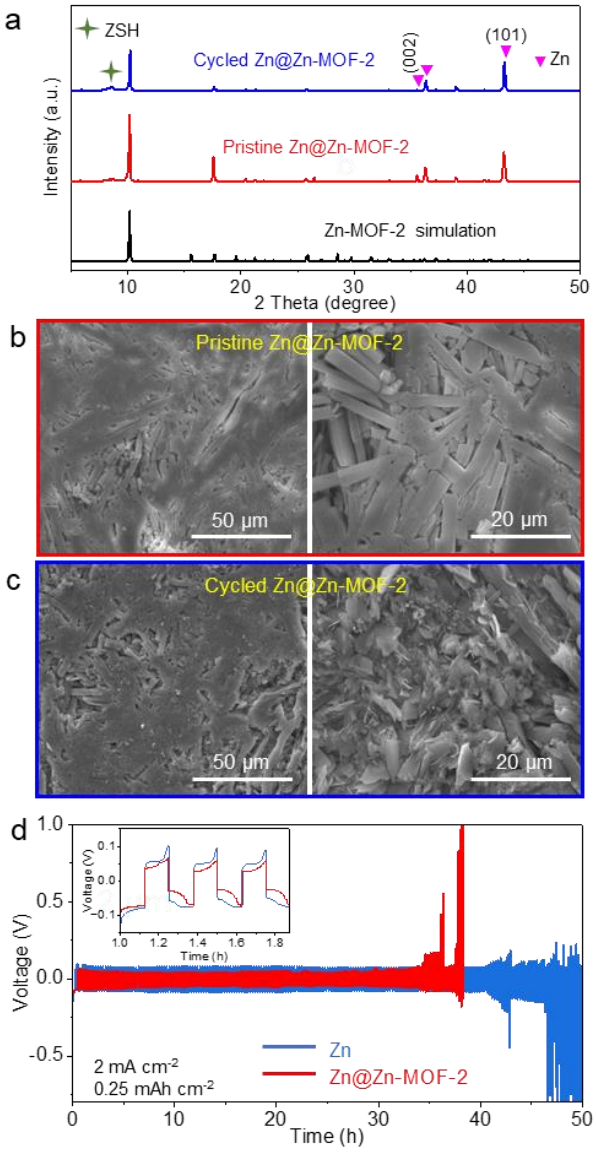

Figure S12. (a) The XRD patterns of zinc foil coated with the Zn-MOF-2 layer (denoted as Zn@Zn-MOF-2) and Zn@Zn-MOF-2 after cycling in $ZnSO_4$. The as-grown Zn-MOF-2 on zinc was well indexed to the standard simulation of Zn-MOF-2. The SEM images of (b) pristine Zn@Zn-MOF-2 and (c) Zn@Zn-MOF-2 after cycling in $ZnSO_4$ for 38 hours. (d) Cycle performance of Zn||Zn and Zn@Zn-MOF-2||Zn@Zn-MOF-2 symmetric cells in pure $ZnSO_4$. The inset in (d) compares the detailed voltage profiles for bare Zn foil and Zn@Zn-MOF-2 in $ZnSO_4$ electrolyte.

Compared to pristine Zn@Zn-MOF-2, the XRD intensity ratio of Zn (002) and Zn (101) is also decreased for Zn@Zn-MOF-2 after cycling in $ZnSO_4$. In addition, the content of Zn-MOF-2 in Zn@Zn-MOF-2 after cycling in $ZnSO_4$ for 38 hours is lower than that in pristine Zn@Zn-MOF-2, indicating the instability of Zn-MOF-2. This is probably because Zn-MOF-2 undergoes a reduction reaction during Zn plating (see evidence in Figure 2c). Moreover, the as-deposited Zn covering on the surface of the Zn-MOF-2 layers is also irregular.

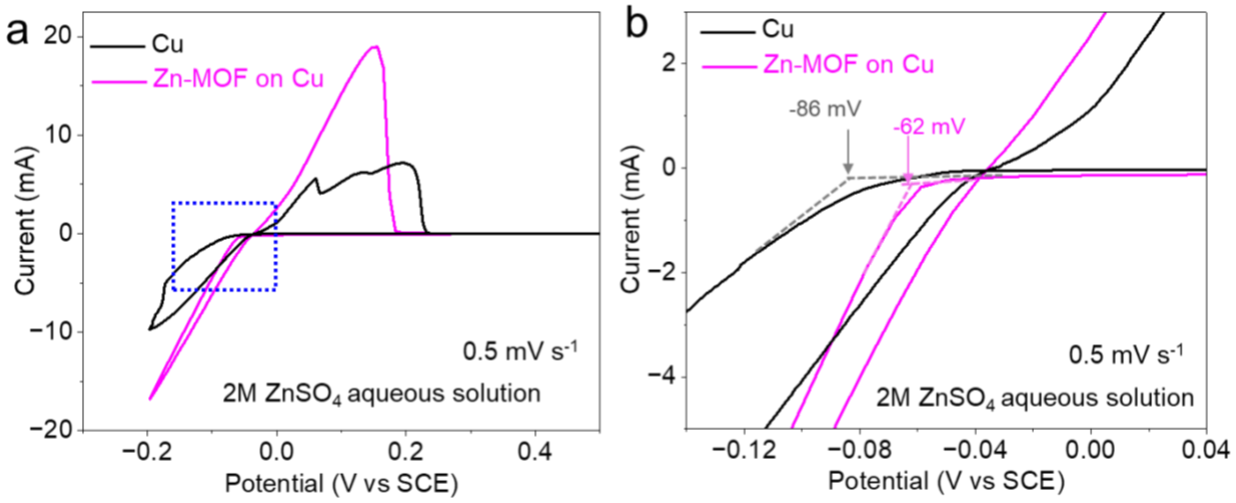

Figure S13. (a) CV curves of bare Cu foil and Zn-MOF loaded on Cu foil in 1 M $ZnSO_4$ aqueous solution. (b) Enlargement of the blue rectangle region in (a).

The CV measurements in Figures S13a and 13b were conducted in a three-electrode electrochemical cell with bare Cu or Zn-MOF loaded Cu as the WE, carbon rod as the CE, and SCE as the RE. Compared to bare Cu, the reduction reaction occurs earlier on the electrode of Zn-MOF loaded Cu, directly indicating that Zn-MOF undergoes reduction ahead of hydrated Zn^{2+} in the electrolyte.

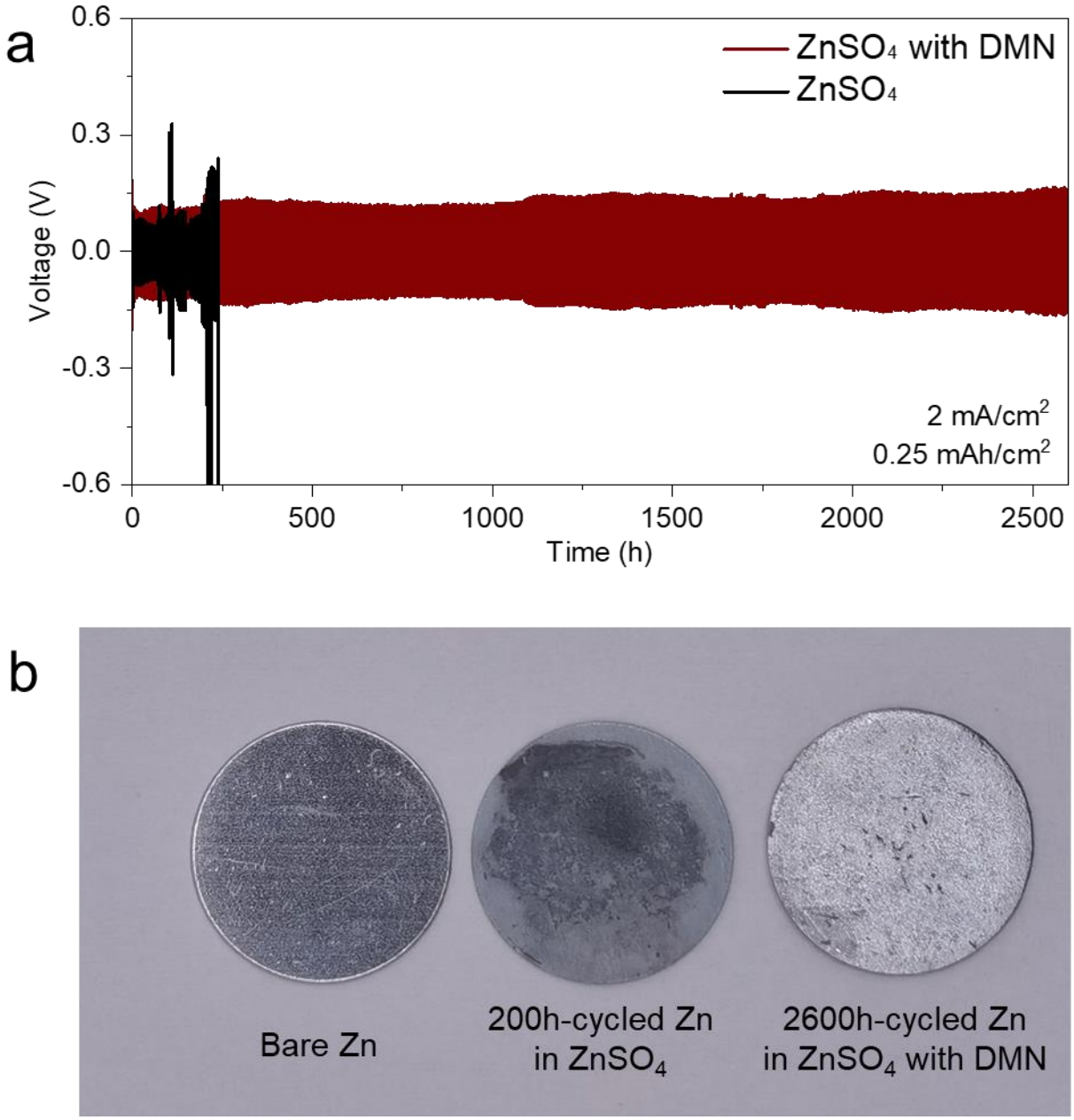

Figure S14. (a) Long-term cycling performance of Zn||Zn symmetric cells in $ZnSO_4$ and $ZnSO_4$ with DMNs respectively. (b) the optical images of bare Zn, Zn cycled in pure $ZnSO_4$, and Zn cycled in $ZnSO_4$ with DMNs.

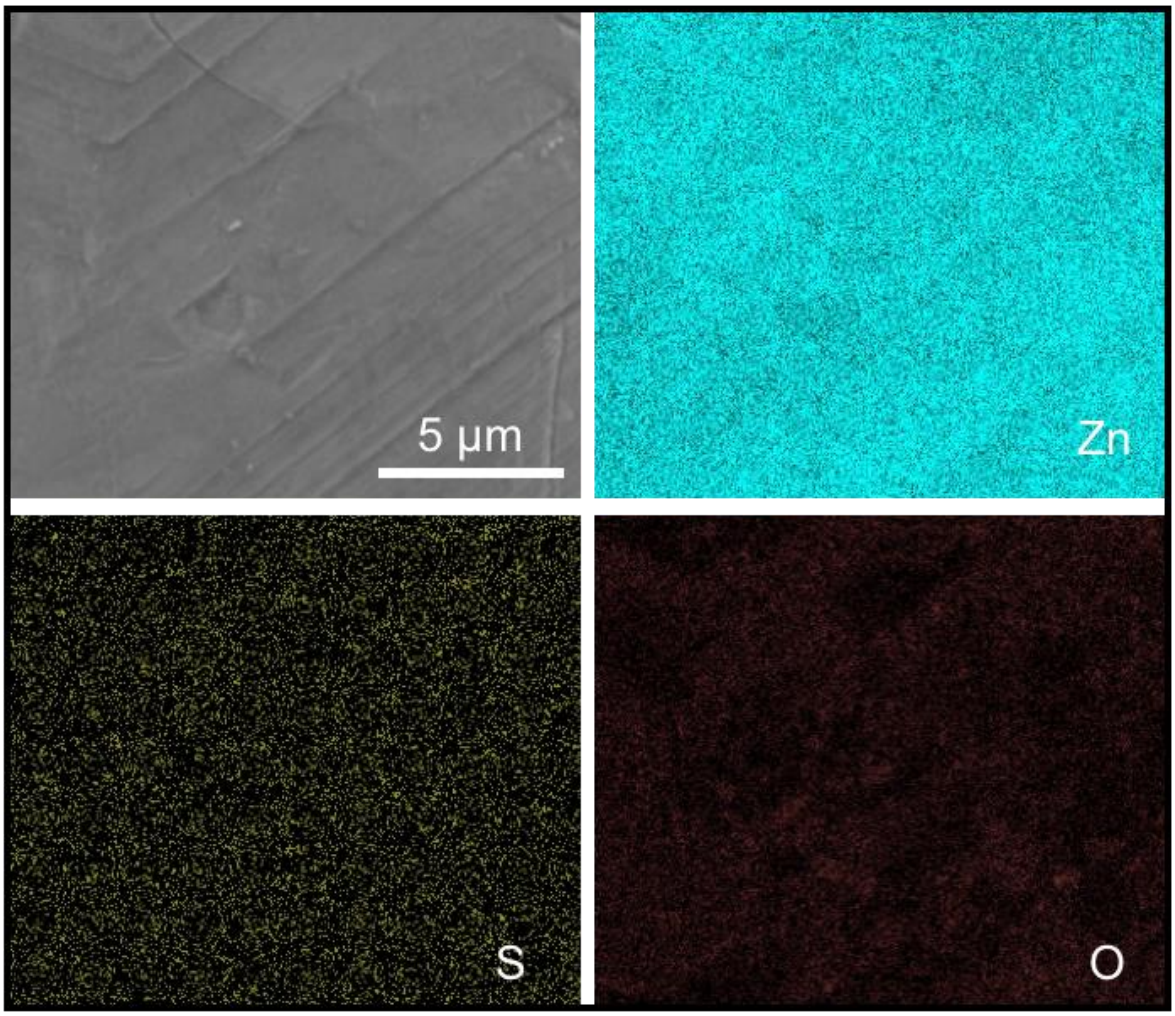

Figure S15. The surface morphology and elemental distribution of Zn, S and O for Zn after cycling in $ZnSO_4$ with DMNs.

There is Zn but no S or O on the surface of the Zn electrode after cycling in $ZnSO_4$ with DMNs.

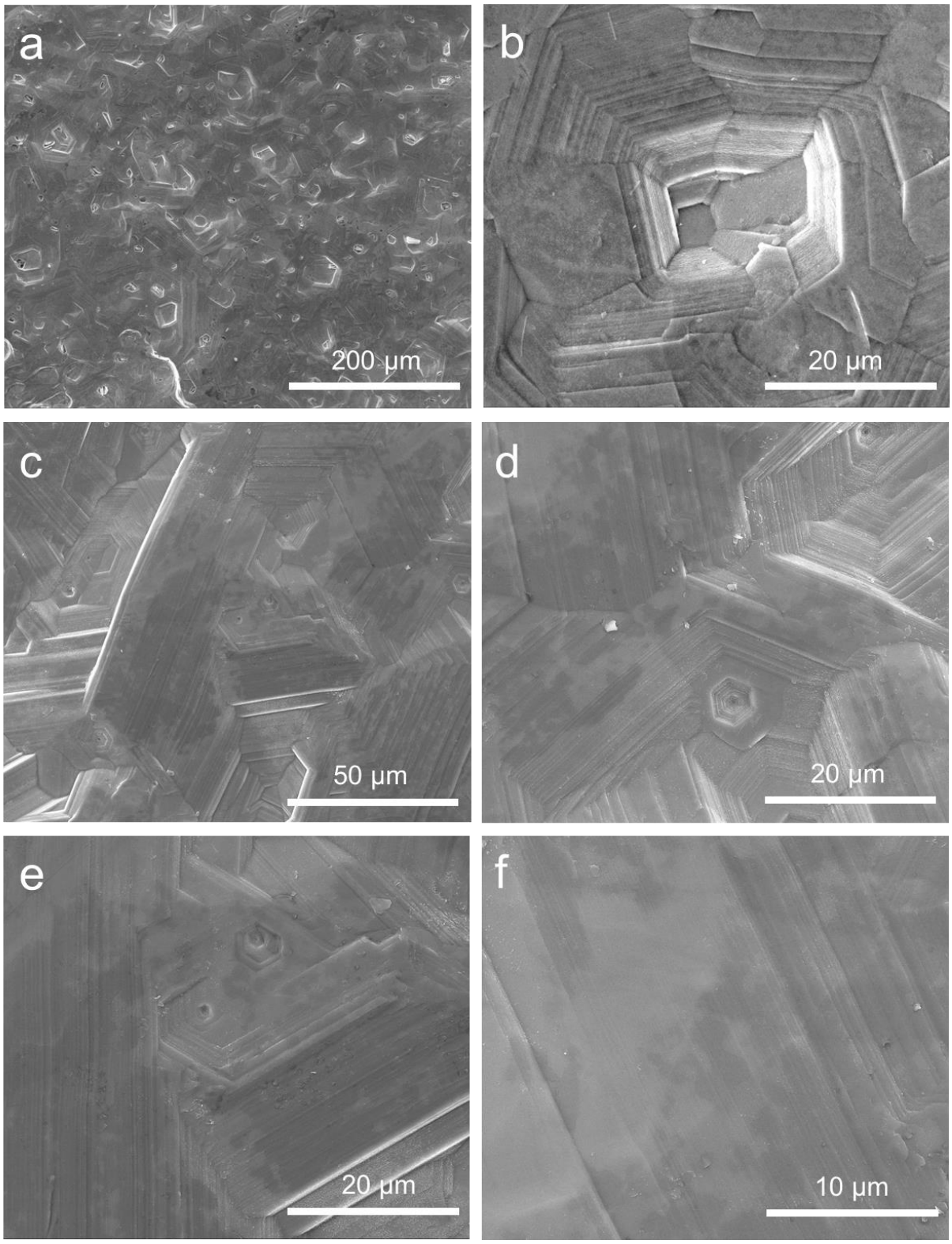

Figure S16. The surface morphology of Zn after cycling in $ZnSO_4$ with DMNs.

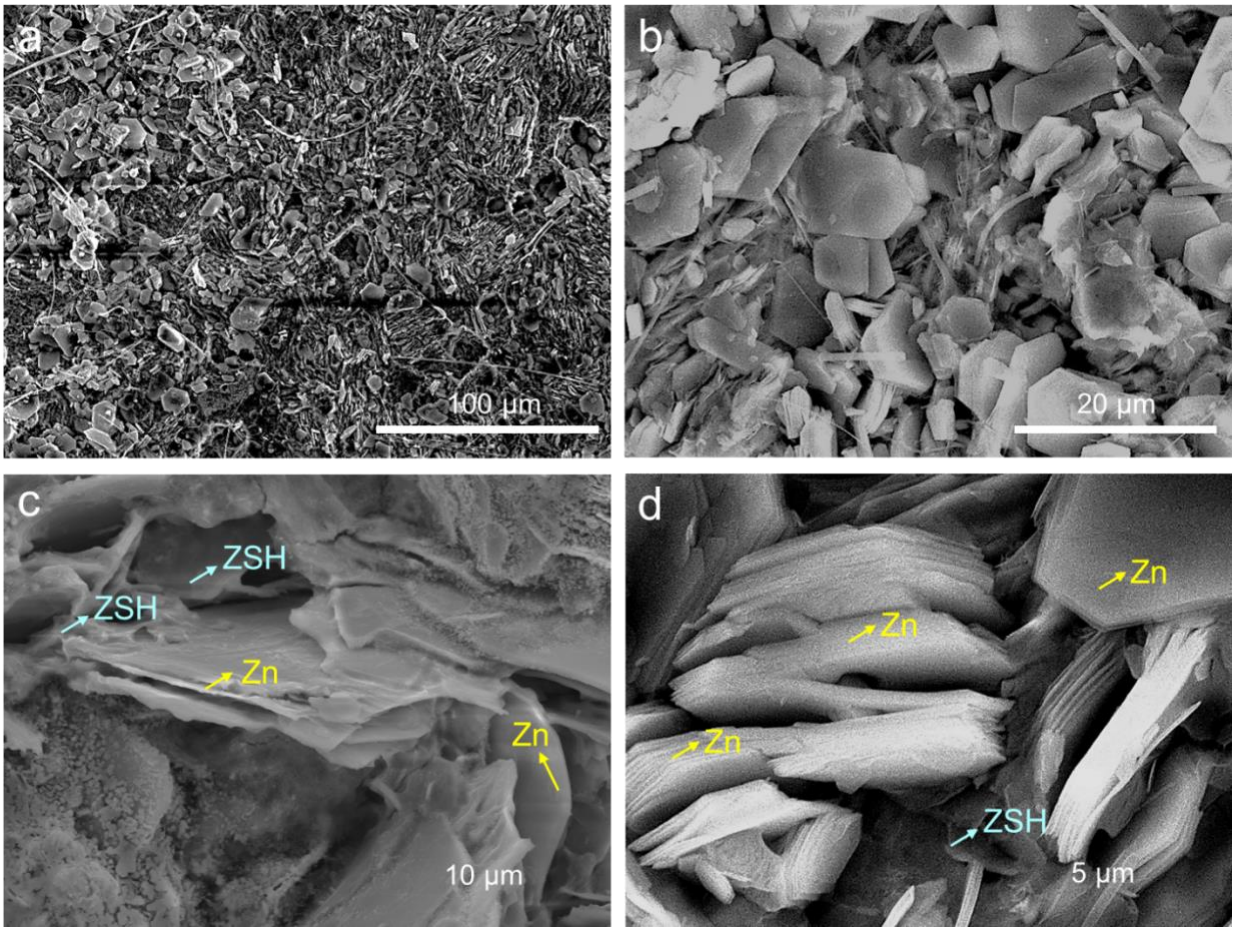

Figure S17. The surface morphology of Zn after cycling in pure $ZnSO_4$.

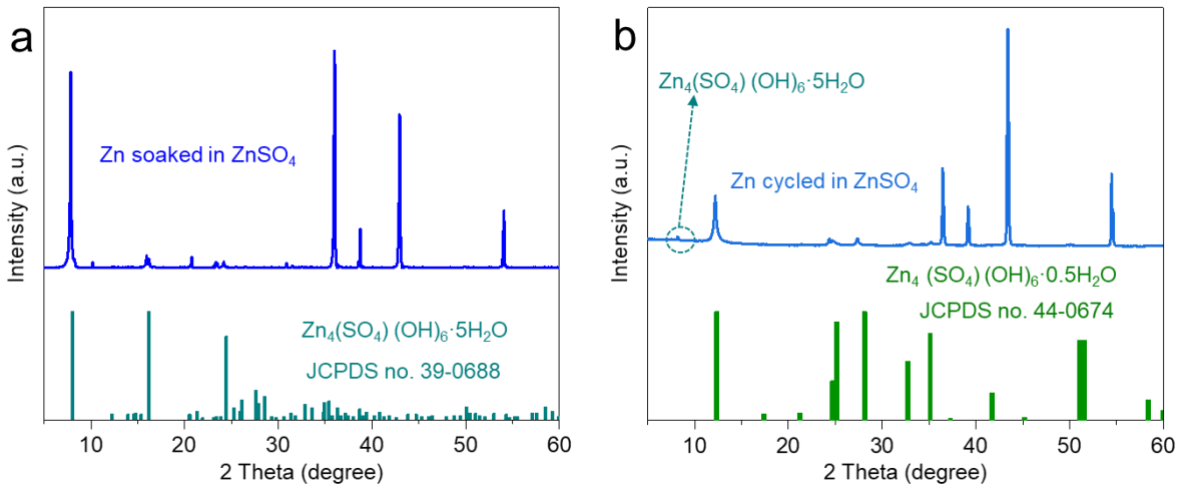

Figure S18. The XRD patterns of (a) Zn soaked in $ZnSO_4$ for 2 weeks and (b) Zn cycled in $ZnSO_4$ for 70 hours at 0.5 mA cm^{-2}. The bottom traces in Figures S18a and 18b are the standard patterns of $Zn_4(SO_4)(OH)_6 \cdot 5H_2O$ (JCPDS no. 39-0688), and $Zn_4(SO_4)(OH)_6 \cdot 0.5H_2O$ (JCPDS no. 44-0674), respectively.

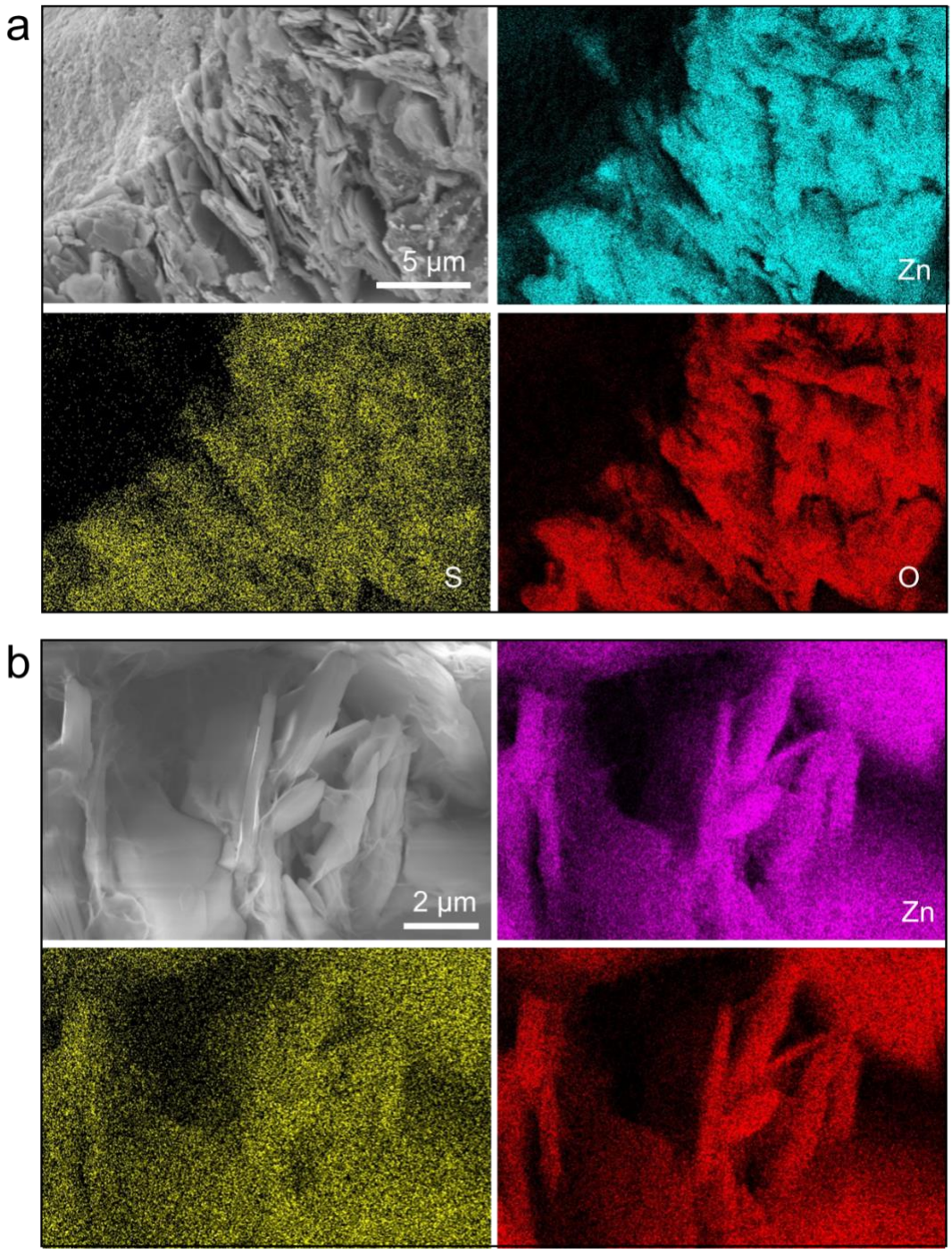

Figure S19. The surface morphology and elemental distribution in two regions of Zn, S and O for Zn after cycling in pure $ZnSO_4$.

There is a large amount of Zn, S and O on the surface of the Zn electrode after cycling in pure $ZnSO_4$.

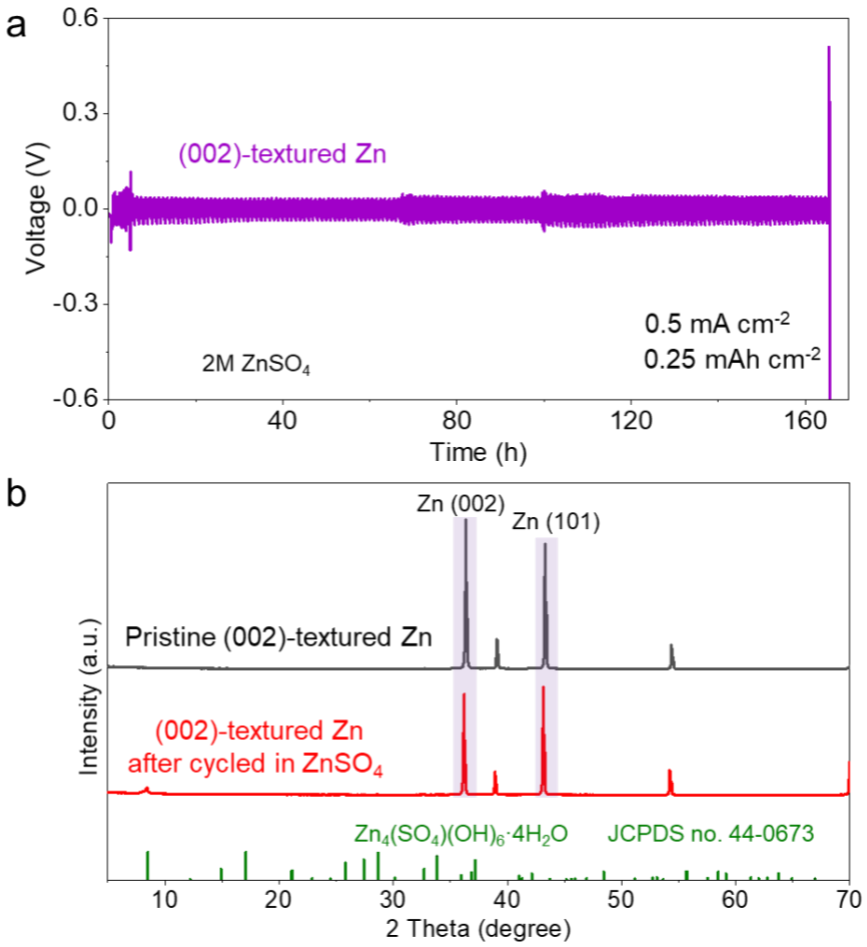

Figure S20. (a) The long-term cycling performance of symmetric cells of (002)-textured Zn in $ZnSO_4$ electrolyte without DMNs. (b) The XRD patterns of pristine (002)-textured zinc foil and (002)-textured zinc foil after cycling in $ZnSO_4$ for 165 hours.

The pristine (002)-textured zinc foil was prepared by polishing bare zinc foil with SiC abrasive paper (2000 mesh) for 1 hour. After cycling (002)-textured zinc in $ZnSO_4$ for approximately 7 days, the (002) orientation decreased accompanied by the formation of the byproduct $Zn_4(OH)_6SO_4{\cdot}4H_2O$ (JCPDS no. 44-0673). It could therefore be concluded that the initial (002)-textured zinc substrate is not able to induce the (002) orientation of subsequent deposited zinc over the cycling.

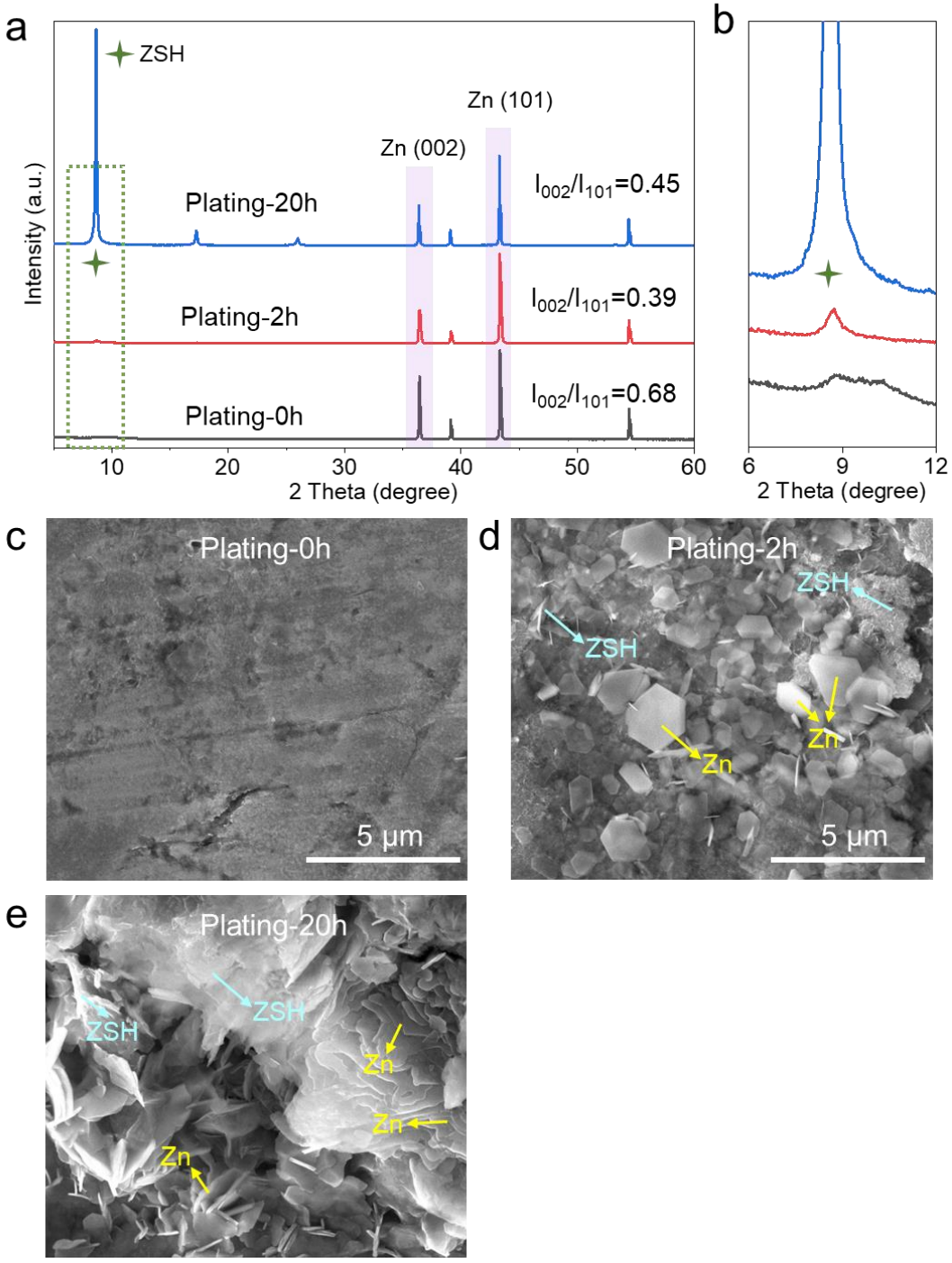

Figure S21. (a) The XRD patterns of Zn foil after different plating times in pure $ZnSO_4$ electrolyte. (b) Enlargement of the green rectangle region in (a). (c-e) SEM images of Zn foil after different plating times in the pure $ZnSO_4$ electrolyte.

The current density of the cell is 0.5 mA cm^{-2}, and the capacity is 0.25 mAh cm^{-2}. A large amount of ZSH byproduct was observed on the surface of the Zn anode with increasing of cycling time, while there was no orientation of the zinc electrodeposits.

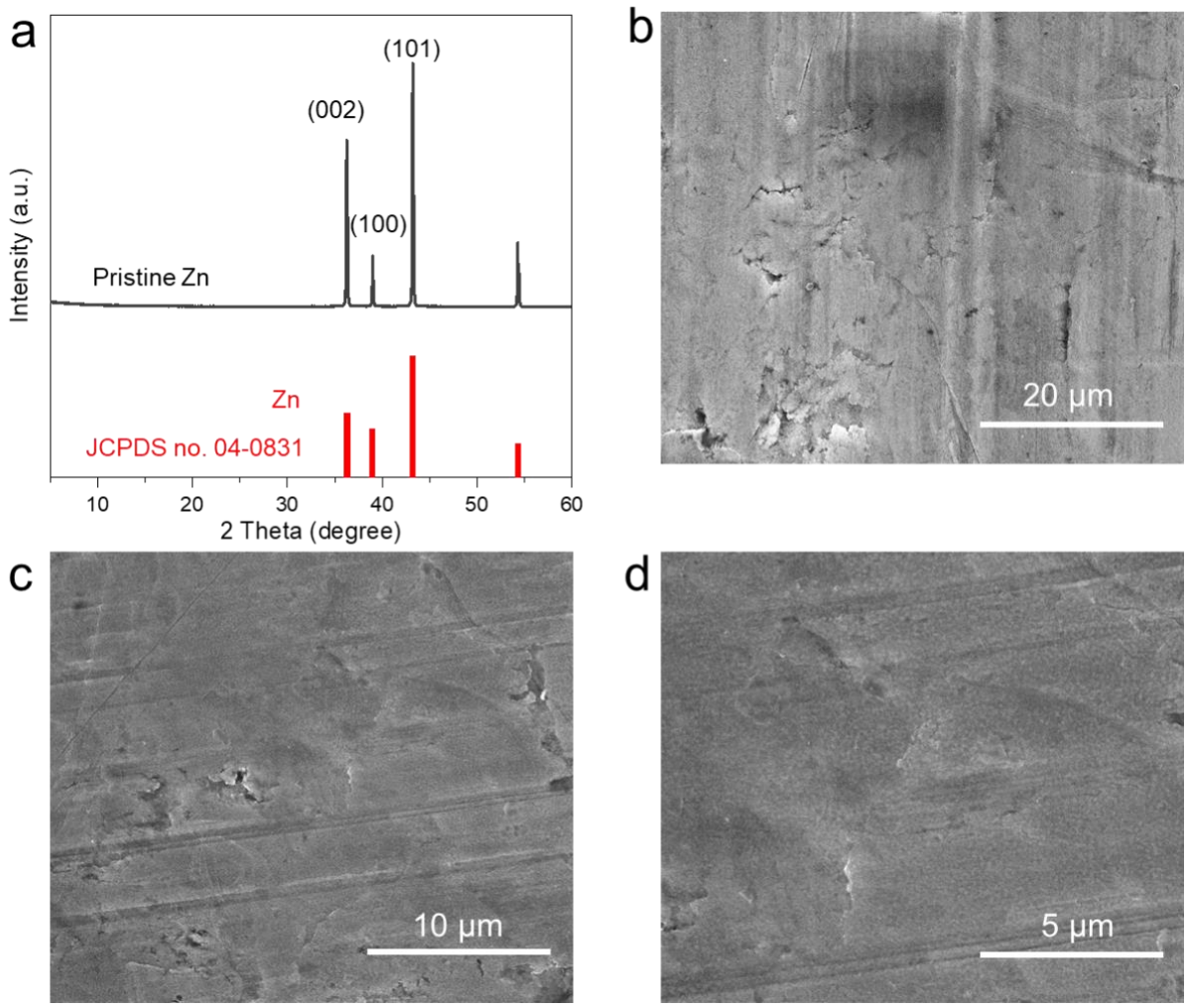

Figure S22. (a) XRD pattern of pristine Zn foil with (101) texture. (b-d) SEM images at different magnifications of pristine Zn foils.

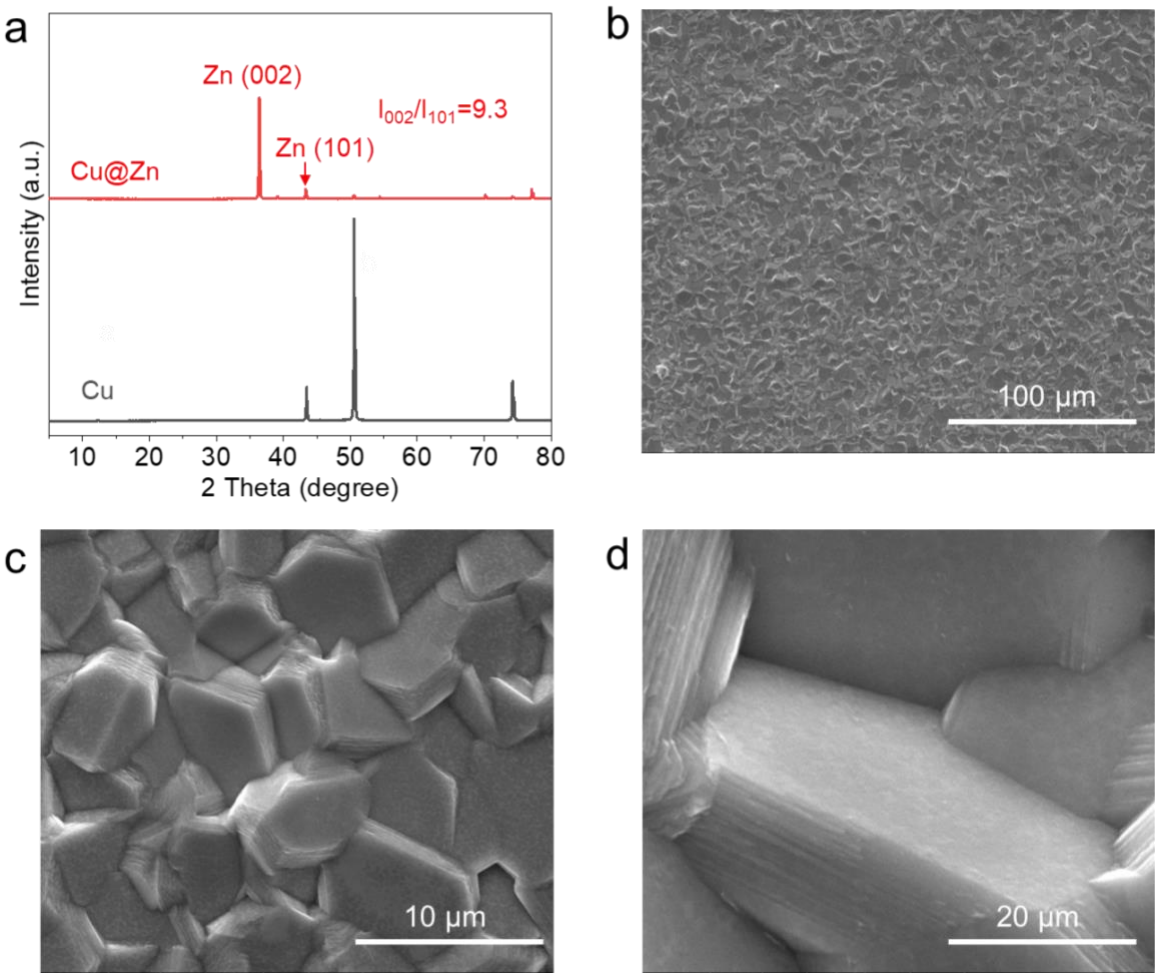

Figure S23. (a) XRD patterns of Cu foil with (002)-textured zinc deposition (denoted as Cu@Zn). (b-d) SEM images at different magnifications of Cu@Zn.

The Cu@Zn was achieved by assembling Cu foil and Zn foil in a coin cell using an electrolyte of $ZnSO_4$ with DMNs. After plating/stripping for 60 hours (0.5 mA cm^{-2}, 0.25 mAh cm^{-2}), (002)-textured zinc deposition was epitaxially grown on the Cu substrate, and no ZSH was detected. The electrodeposited zinc flakes were stacked layer by layer, forming an even surface.

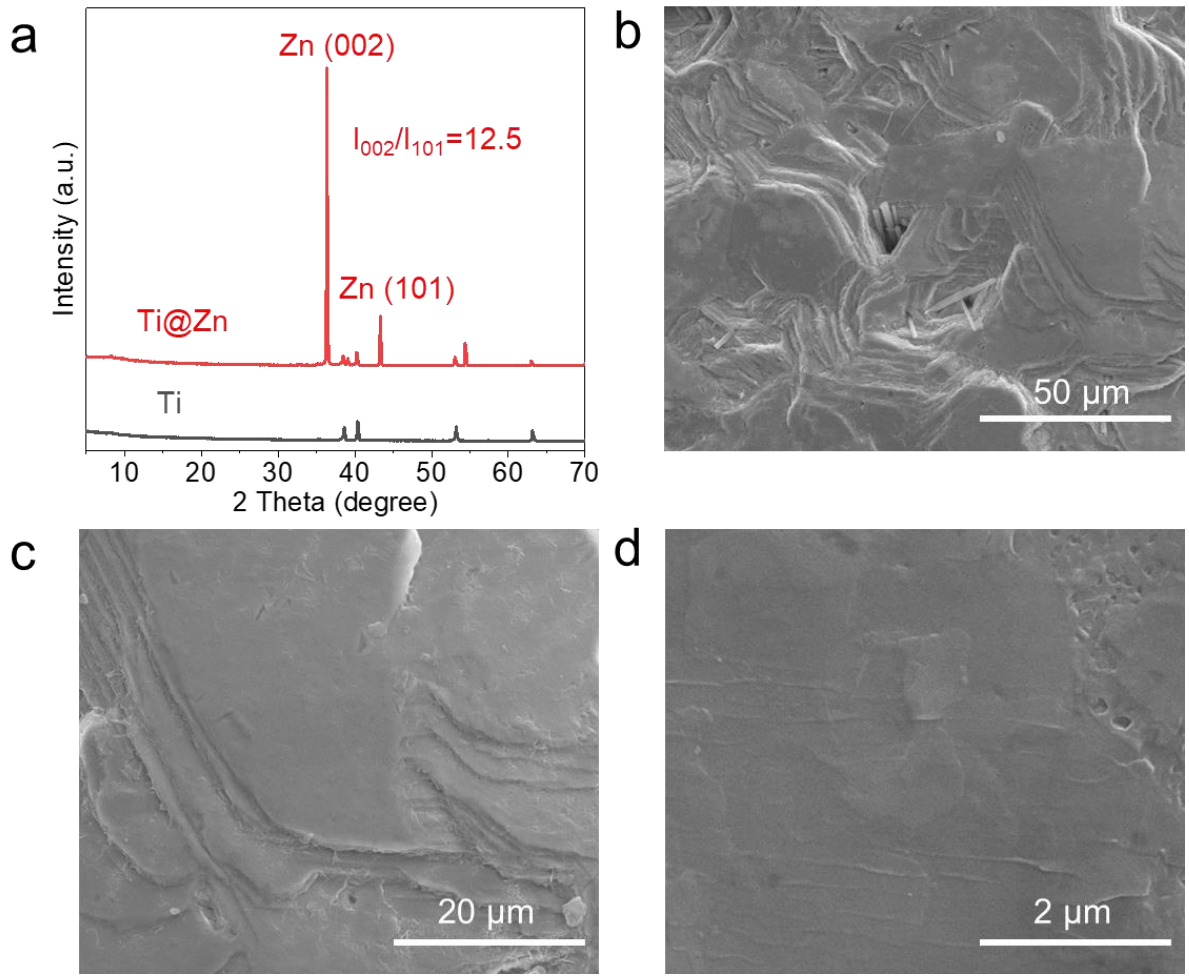

Figure S24. (a) XRD patterns of Ti foil with (002)-textured zinc deposition (denoted as Ti@Zn). (b-d) SEM images at different magnifications of Ti@Zn.

The Ti@Zn was achieved by assembling Ti foil and zinc foil in a coin cell using an electrolyte of $ZnSO_4$ with DMNs. After plating/stripping for 60 hours (0.5 mA cm^{-2}, 0.25 mAh cm^{-2}), (002)-textured zinc deposition was epitaxially grown on the Ti substrate, and no ZSH was detected. The electrodeposited zinc flakes were aligned horizontally, generating a smooth surface.

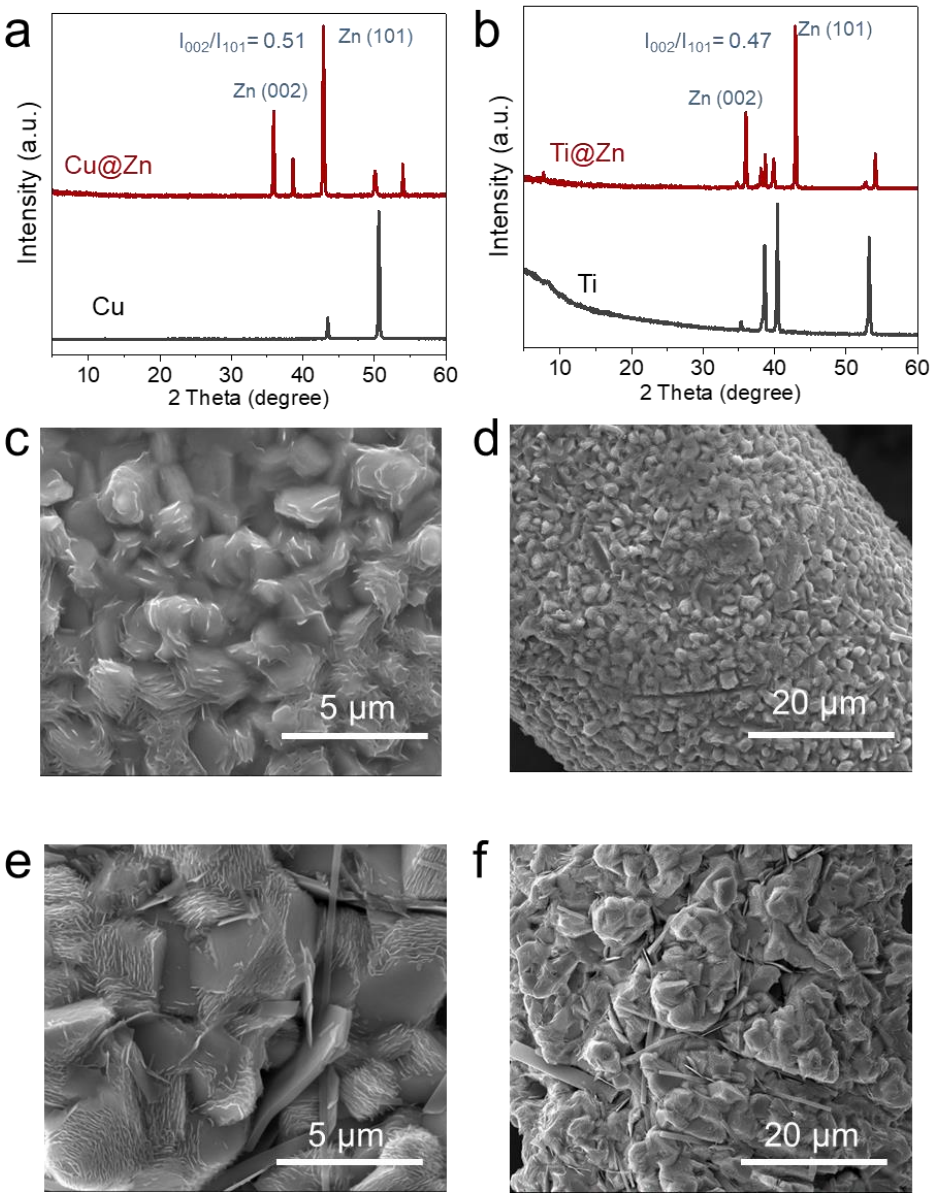

Figure S25. (a, b) XRD patterns of Cu mesh and Ti mesh after Zn deposition with DMNs (denoted as Cu@Zn and Ti@Zn). (c, d) SEM image of Cu@Zn. (e, f) SEM images of Ti@Zn.

After 20 hours' deposition at 0.5 mA cm^{-2} with DMNs, the rough surface of metal mesh (Cu and Ti), which induces randomly aligned DMNs, is deposited by randomly aligned zinc plates.

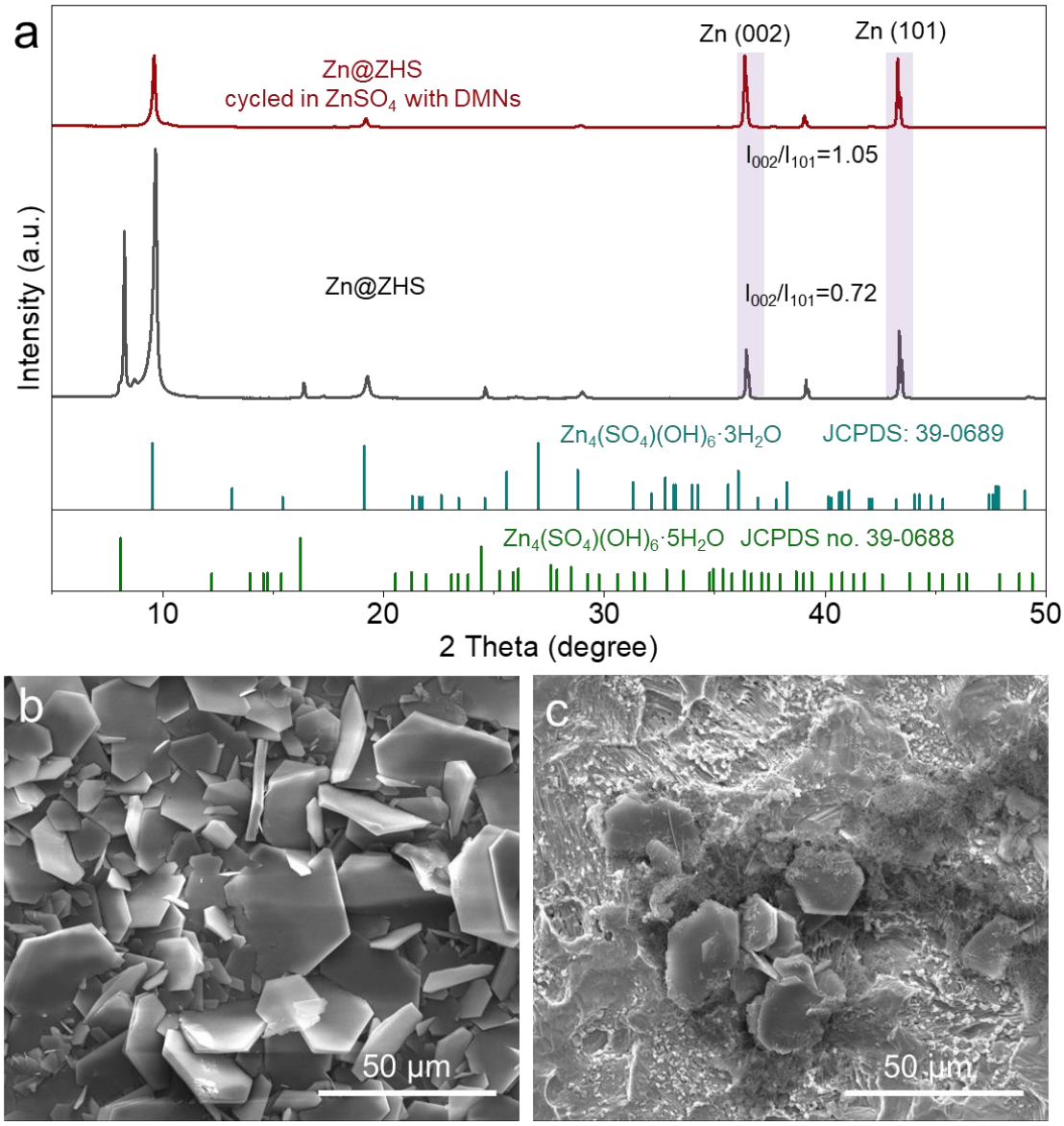

Figure S26. (a) The XRD patterns of Zn foil after soaking in $ZnSO_4$ (2 M) solution for 30 days (denoted as ZSH coated Zn) and ZSH coated Zn after cycling in $ZnSO_4$ with DMNs for 3 days. SEM images of (b) ZSH coated Zn and (c) ZSH coated Zn after cycling in $ZnSO_4$ with DMNs for 3 days.

The XRD pattern of ZSH coated Zn was well indexed to a mix of $Zn_4(OH)_6SO_4·5H_2O$ (JCPDS no. 39-0688), $Zn_4(OH)_6SO_4·3H_2O$ (JCPDS no. 39-0689) and zinc metal. After cycling ZSH coated Zn in $ZnSO_4$ with DMNs, $Zn_4(OH)_6SO_4·5H_2O$ with a larger layer spacing was transformed priorly, leaving a much-weakened intensity of $Zn_4(OH)_6SO_4·3H_2O$. Compared to ZSH coated Zn, the (002) orientation of ZSH coated Zn after cycling was also strengthened. The initial surface of ZHS coated Zn was full of huge hexagonal ZSH flakes, while hexagonal ZSH flakes were obviously decreased after cycling ZSH coated Zn in $ZnSO_4$ with DMNs. In addition, much of the Zn surface was exposed after cycling ZSH coated Zn in $ZnSO_4$ with DMNs.

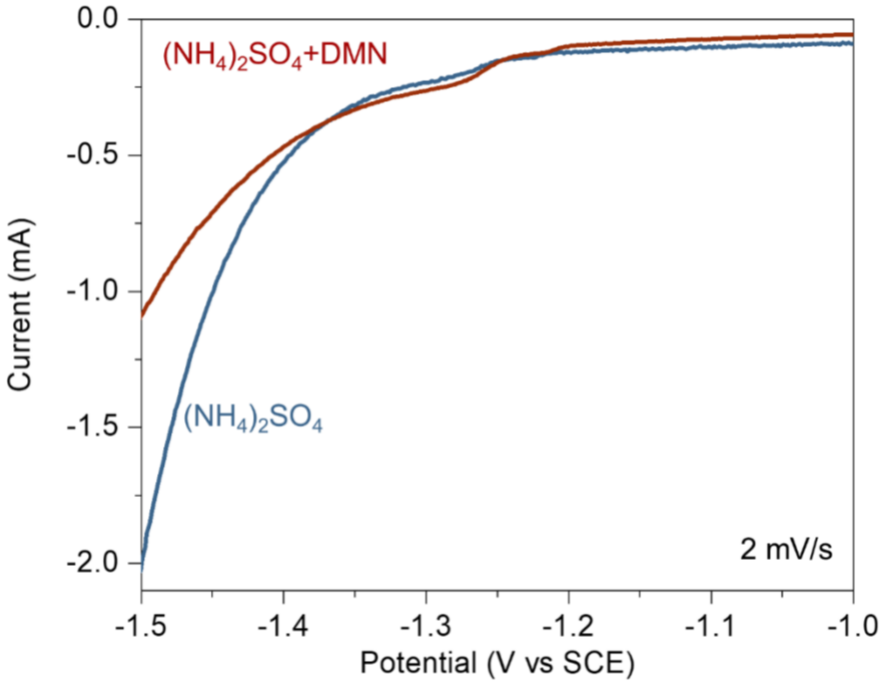

Figure S27. Linear sweep voltammetry (LSV) curves of Ti foils in 1 M $(NH_4)_2SO_4$ solution with and without DMNs, respectively.

The LSV measurements were carried out using a three-electrode electrochemical cell, with Ti foils serving as the working electrode (WE), a carbon rod as the counter electrode (CE), and a saturated calomel electrode (SCE) as the reference electrode (RE). The scanning rate employed was 2 mV s^{-1}. DMNs were introduced into the $(NH_4)_2SO_4$ solution by directly dispersing DMNs powders, which were obtained from the $ZnSO_4$ electrolyte containing DMNs. The addition of DMNs resulted in a notable reduction in the current for hydrogen evolution reaction (HER), decreasing from 2 mA to 1.1 mA at the potential of -1.5 V (vs SCE). This observation suggests that DMNs possess the capability to suppress HER, possibly by effectively covering the surface of electrodes and repelling water within the electric double layers.

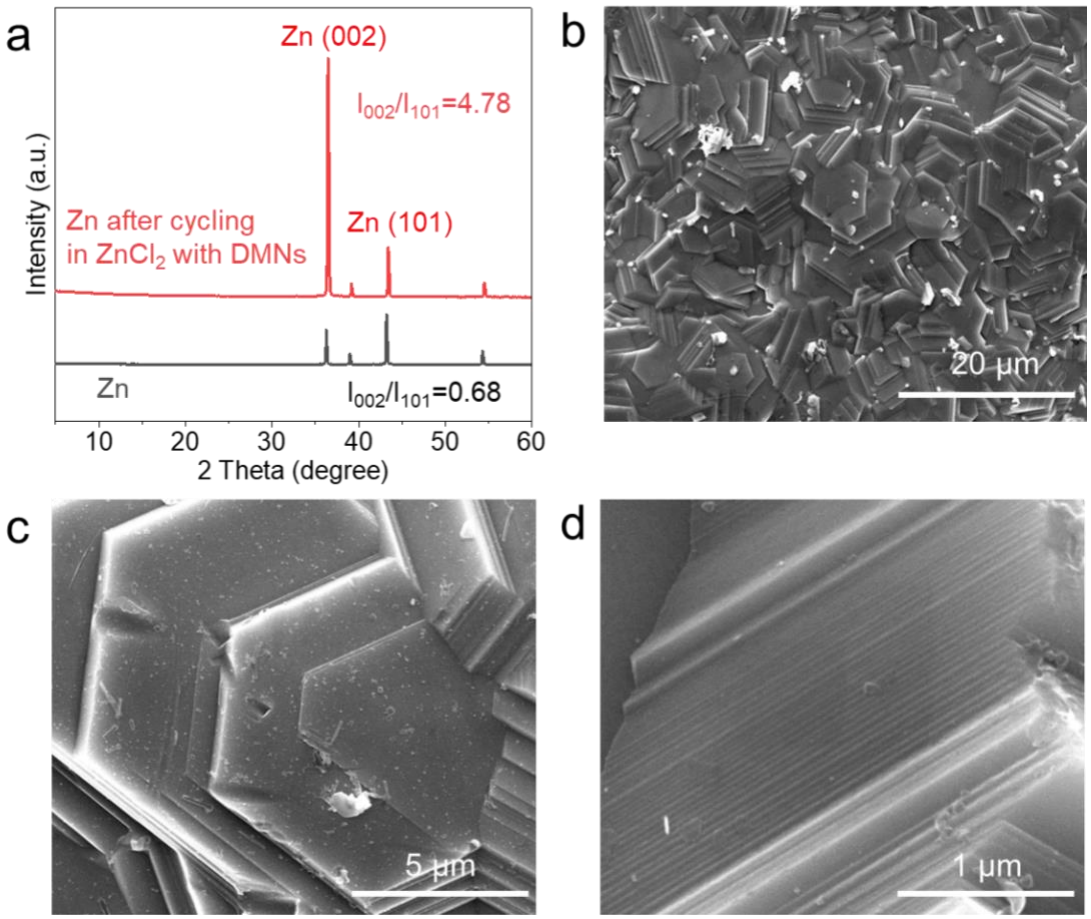

Figure S28. (a) XRD patterns of bare Zn foil and Zn foil after cycling in $ZnCl_2$ with DMNs. (b-d) SEM images at different magnifications of zinc foil after cycling in $ZnCl_2$ with DMNs.

The preparation of a solution of $ZnCl_2$ with DMNs is similar to that for the $ZnSO_4$ electrolyte, which is afore mentioned in the Methods, with simply replacing 2 M $ZnSO_4$ with 2 M $ZnCl_2$. After plating/stripping for 20 hours in zinc symmetric cells (0.5 mA cm^{-2}, 0.25 mAh cm^{-2}), the zinc foil shows an enhanced (002) zinc orientation in the absence of ZSH. The horizontal hexagonal zinc flakes are stacked layer by layer, forming a compact surface.

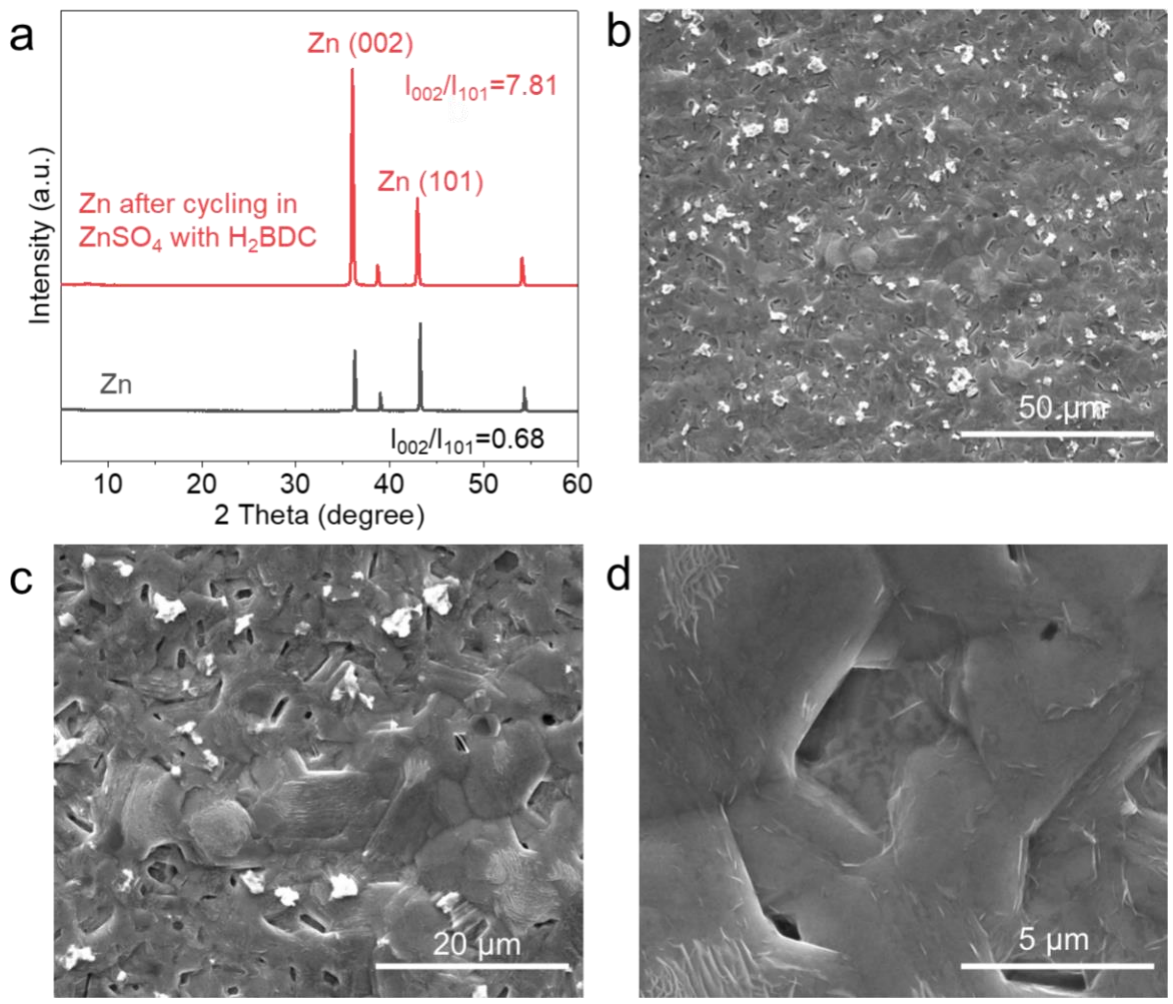

Figure S29. (a) XRD patterns of bare Zn foil and Zn foil after cycling in $ZnSO_4$ with H_2BDC. (b-d) SEM images at different magnifications of zinc foil after cycling in $ZnSO_4$ with H_2BDC.

By substituting H_2BDC for H_3BTC and dimethylformamide (DMF) for ethanol, the DMN-regulated method in the Methods could well expand to other ligands. After plating/stripping for 250 hours in zinc symmetric cells (0.5 mA cm^{-2}, 0.25 mAh cm^{-2}), the zinc foil demonstrated an enhanced (002) zinc orientation and the absence of ZSH. The Zn is homogeneously deposited on the Zn anode by forming a flat surface.

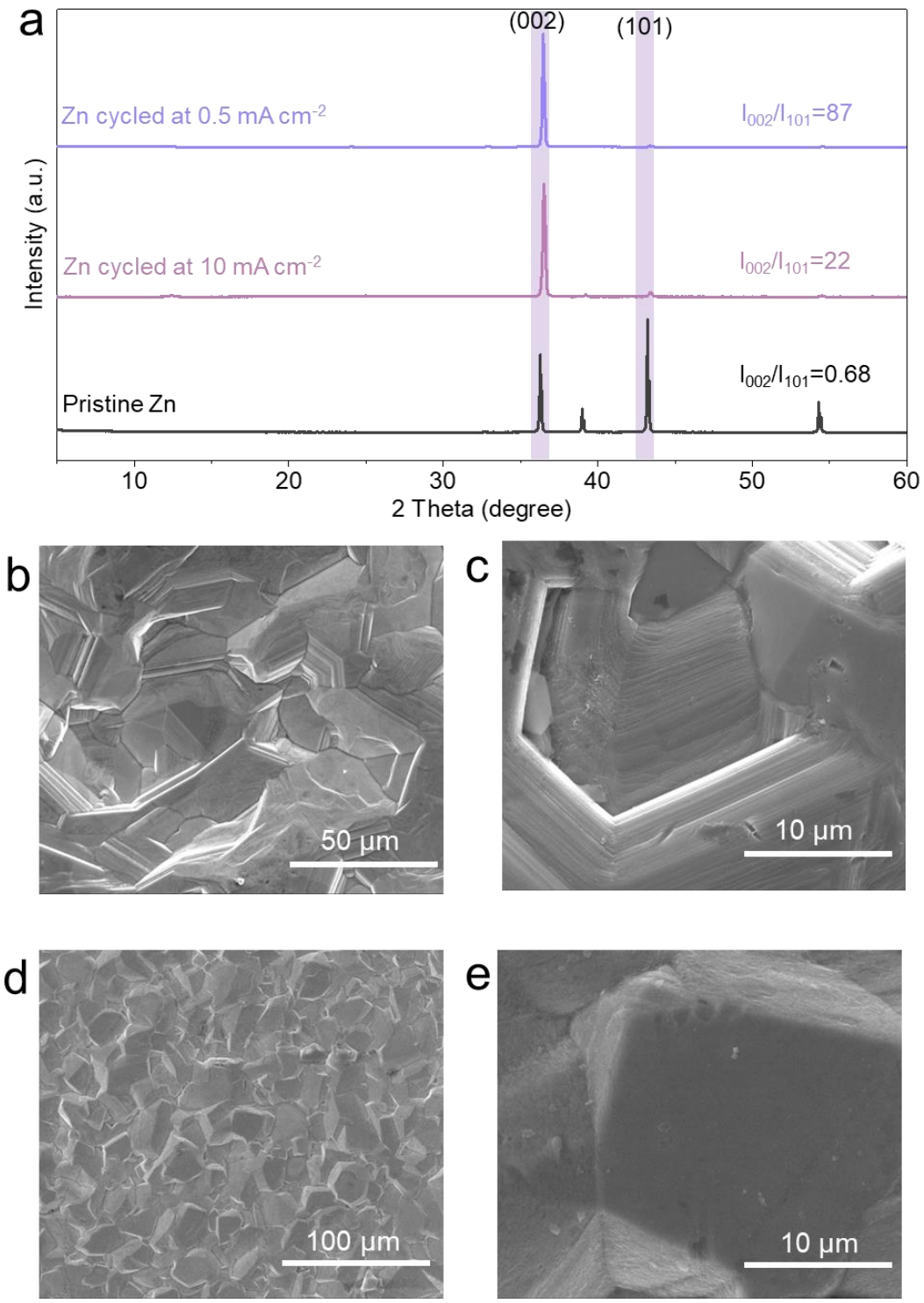

Figure S30. (a) XRD patterns of pristine Zn foil and Zn after cycling in the electrolyte of $ZnSO_4$ with DMNs at 0.5 mA cm^{-2} and 10 mA cm^{-2}, respectively. SEM images of Zn after cycling in the electrolyte of $ZnSO_4$ with DMNs at (b, c) 2 mA cm^{-2} and (d, e) 10 mA cm^{-2}.

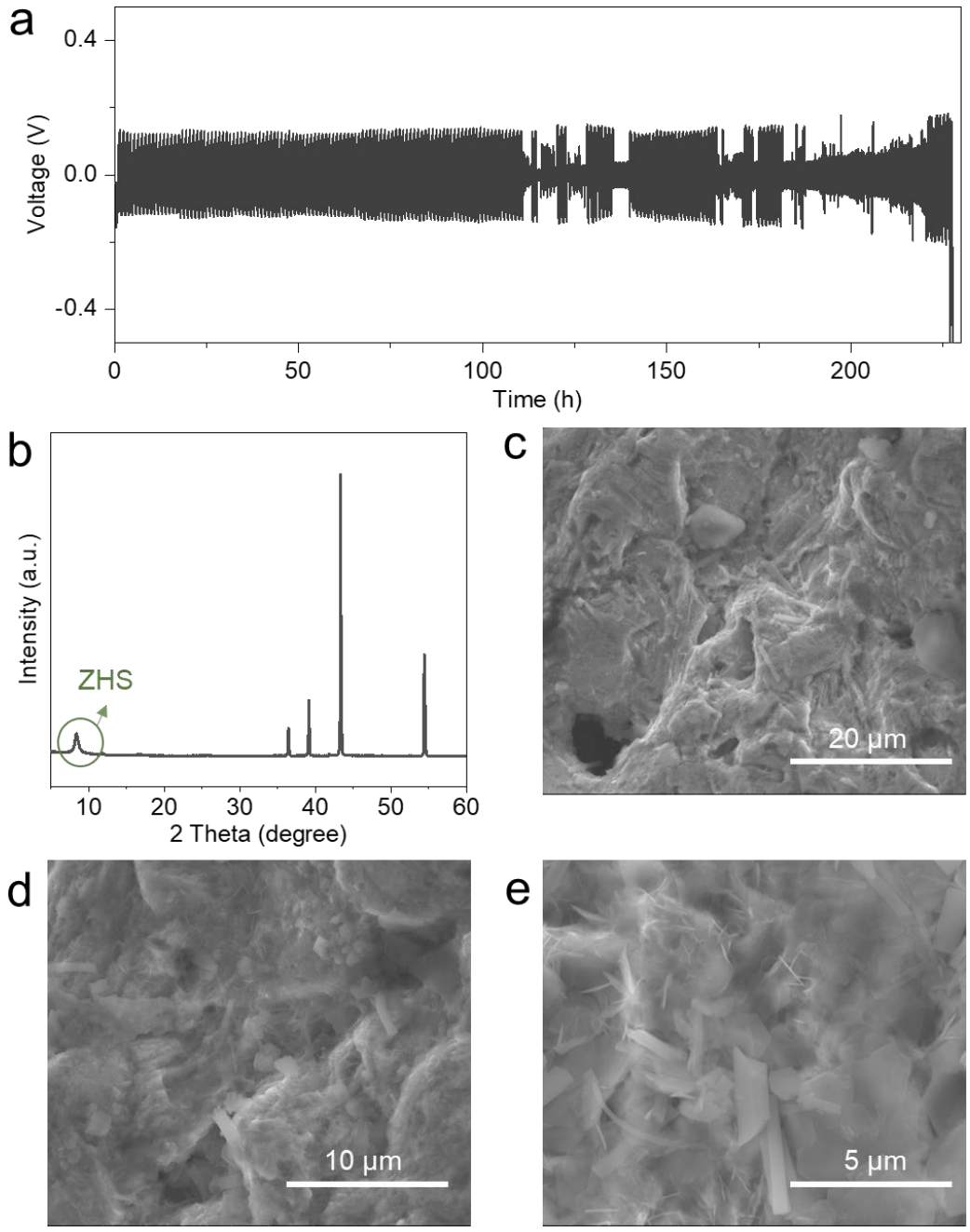

Figure S31. (a) Long-term cycling performance of Zn||Zn symmetric cells in 2 M $ZnSO_4$ with minor ethanol (no ligands) at a current density of 0.5 mA cm^{-2} and capacity of 0.25 mAh cm^{-2}. (b) XRD patterns and (c-e) SEM images of Zn electrode after cycling in the $ZnSO_4$ electrolyte containing minor ethanol.

The Zn||Zn symmetric cells operating in 2 M $ZnSO_4$ electrolytes with a water-ethanol mixture (EtOH: 20%, v/v) as the solvents demonstrated unsatisfactory cycling performance. After cycling, the obtained zinc foils lacked (002)-texturing and retained byproducts, displaying loosely deposited zinc. Consequently, the addition of ethanol dissolving ligands had minimal impact on enhancing zinc anode protection.

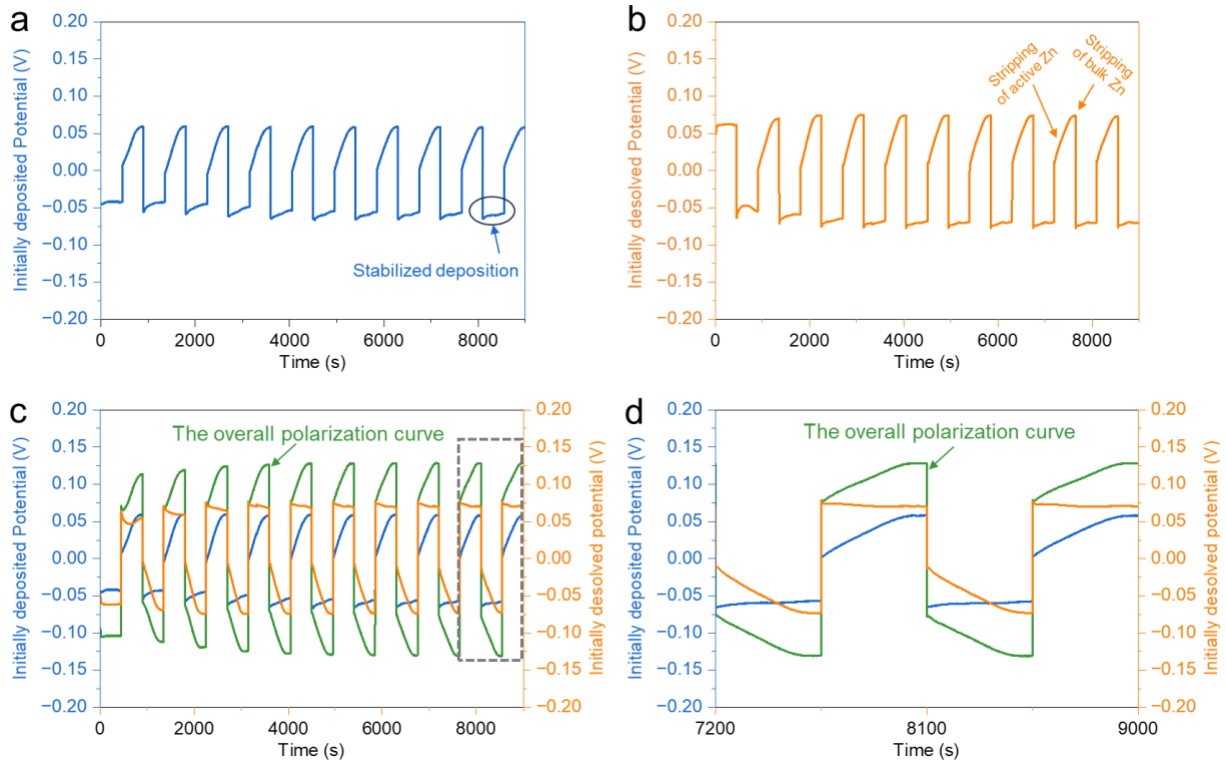

Figure S32. (a, b) Plating and stripping curves of two Zn foil electrodes (including WE and CE) in symmetric cell using three electrode system (WE: Zn foil, CE: Zn foil, RE: Zn ring) in 2 M $ZnSO_4$ electrolyte with DMNs at 2 mA cm^{-2}. (c) The overall polarization curve by coupling (a) and (b). (d) The enlargement of steady-state cycling curves from the grey rectangle in (c).

In Zn||Zn symmetric cells, the polarization voltage is a combination of the plating and stripping processes. To analyze these processes individually, a reference electrode of Zn ring is introduced into the symmetric cells. Then, the time-voltage profiles of two Zn foil electrodes (namely working electrode and counter electrode) within the same symmetric cell are monitored: one was initially deposited and the other is initially dissolved.

During the initial cycles, the overpotential for the plating process consistently decreases. The plating curves gradually flattens and stabilizes, indicating a robust and conformal deposition process. The higher deposition overpotential compared to Fig. S33 suggests a more intense nucleation process when DMNs are present.

On the other hand, the overpotential for the stripping process can be divided into two parts: the electrodeposited active Zn and the bulk Zn. The compactly electrodeposited Zn with (002)-orientation is more resistant to dissolution, resulting in higher stripping potential, compared to the situation depicted in Fig. S33. Consequently, the overall polarization curve appears smoother with relatively fewer voltage fluctuations.

These observations highlight the beneficial impact of DMNs, leading to improved and controlled plating and stripping processes, as well as a more stable and uniform Zn surface morphology.

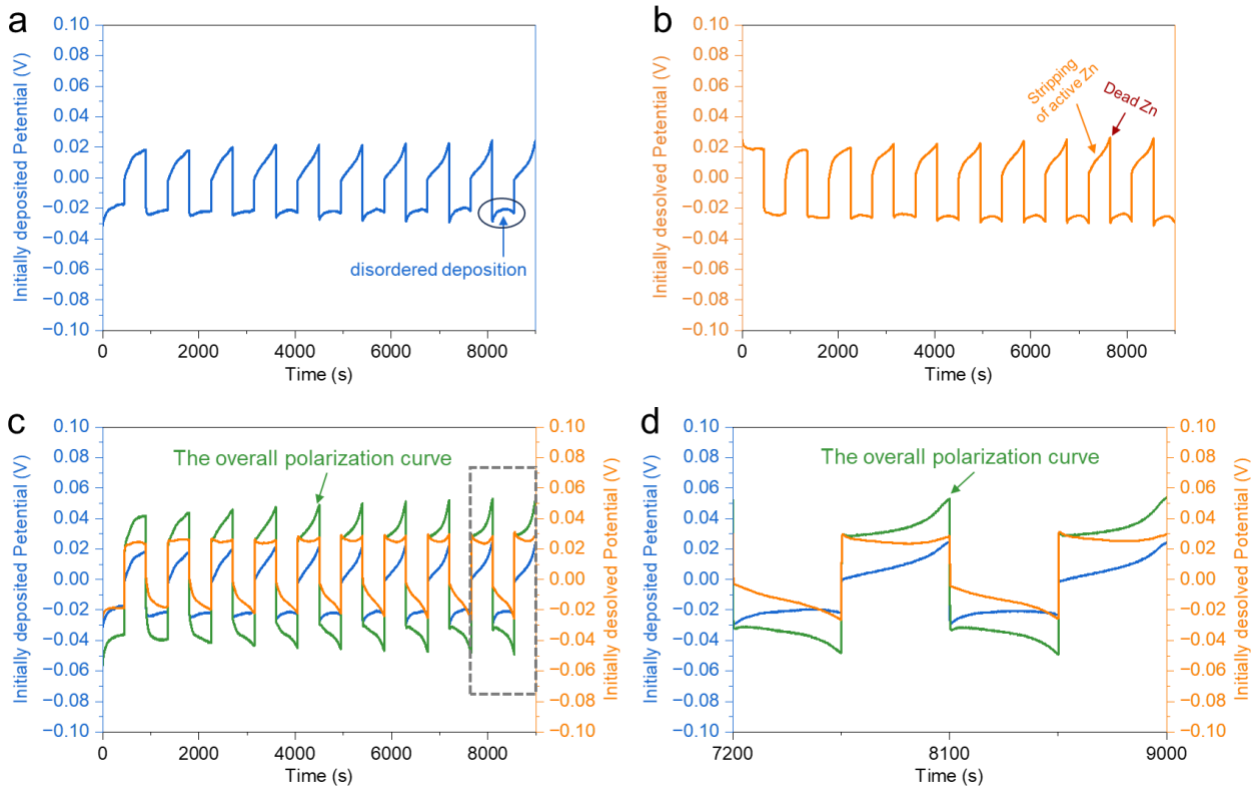

Figure S33. (a, b) Plating and stripping curves of two Zn foil electrodes (including WE and CE) in symmetric cell using three electrode system (WE: Zn foil, CE: Zn foil, RE: Zn ring) in 2 M $ZnSO_4$ electrolyte without DMNs at 2 mA cm^{-2}. (c) The overall polarization curve by coupling (a) and (b). (d) The enlargement of steady-state cycling curves from the grey rectangle in (c).

Throughout all cycles, the plating curves consistently show a slight crookedness over time, suggesting a gradually disordered deposition process. The deposition overpotential is merely half of what is observed with DMNs (Fig. S32), aligning with the characteristics of porous and mossy Zn deposits. In the stripping process, the overpotential initially involves the dissolution of bulk Zn, but this contribution diminishes in subsequent cycles. The loosely electrodeposited Zn is more susceptible to dissolution, leading to the gradual disappearance of bulk Zn dissolution. Unfortunately, a rapid rise in the stripping curves occurs with cycling, mainly due to contact loss between the electrodeposited zinc and bulk Zn, resulting in the formation of "dead Zn".[5] This phenomenon further contributes to the erratic behavior of the overall polarization curve, resulting in substantial voltage fluctuations.

These findings underscore the significance of DMNs in promoting more ordered and stable deposition processes and mitigating issues related to dead Zn, ultimately leading to a smoother polarization curve with reduced voltage fluctuations.

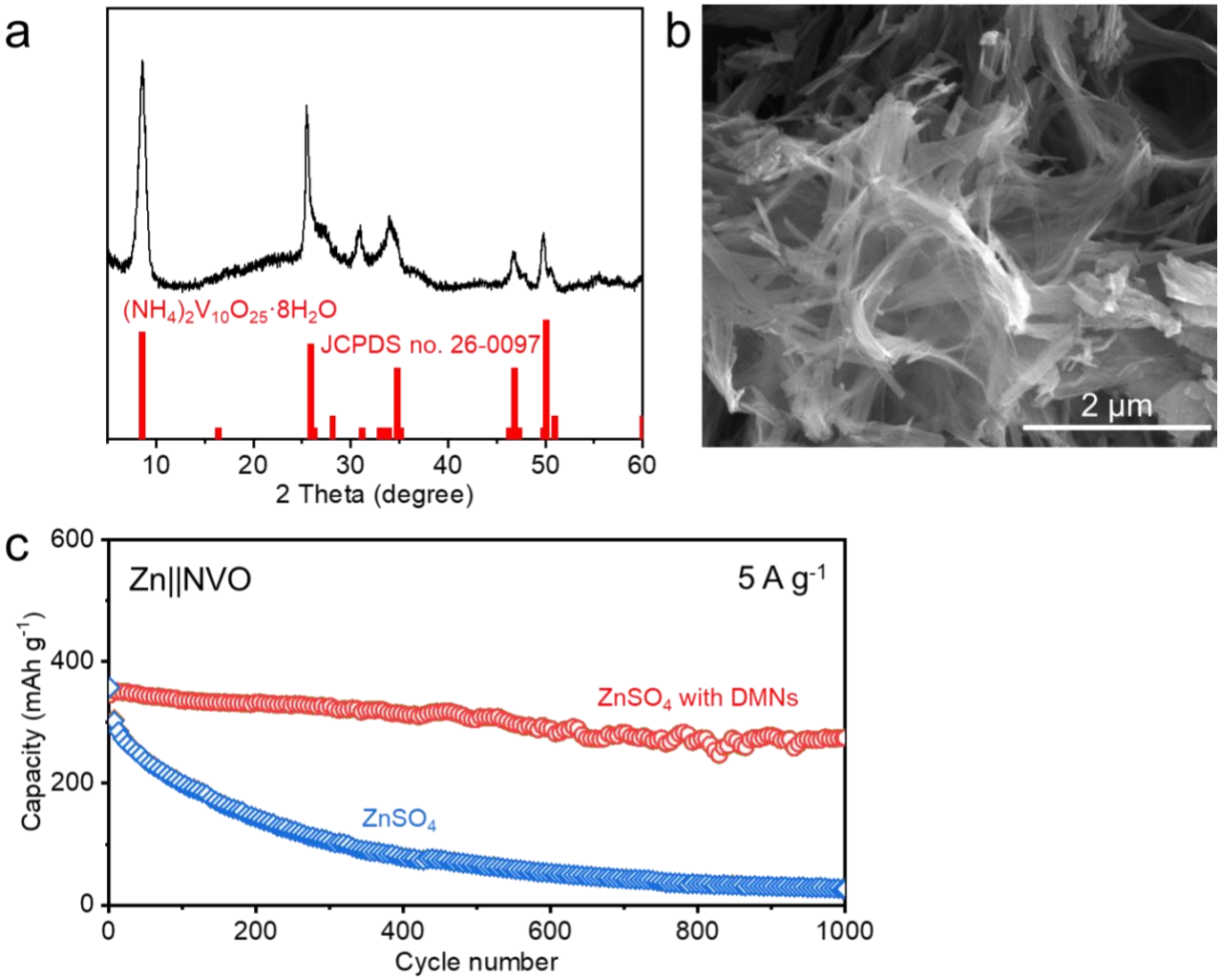

Figure S34. (a) XRD pattern and (b) SEM image of as-prepared $(NH_4)_2V_{10}O_{25}\cdot 8H_2O$ (denoted as NVO) powders. (c) The cyclic stability of Zn||NVO full cells at a current density of 10 A g^{-1} in the electrolytes of pure $ZnSO_4$ and $ZnSO_4$ with DMNs.

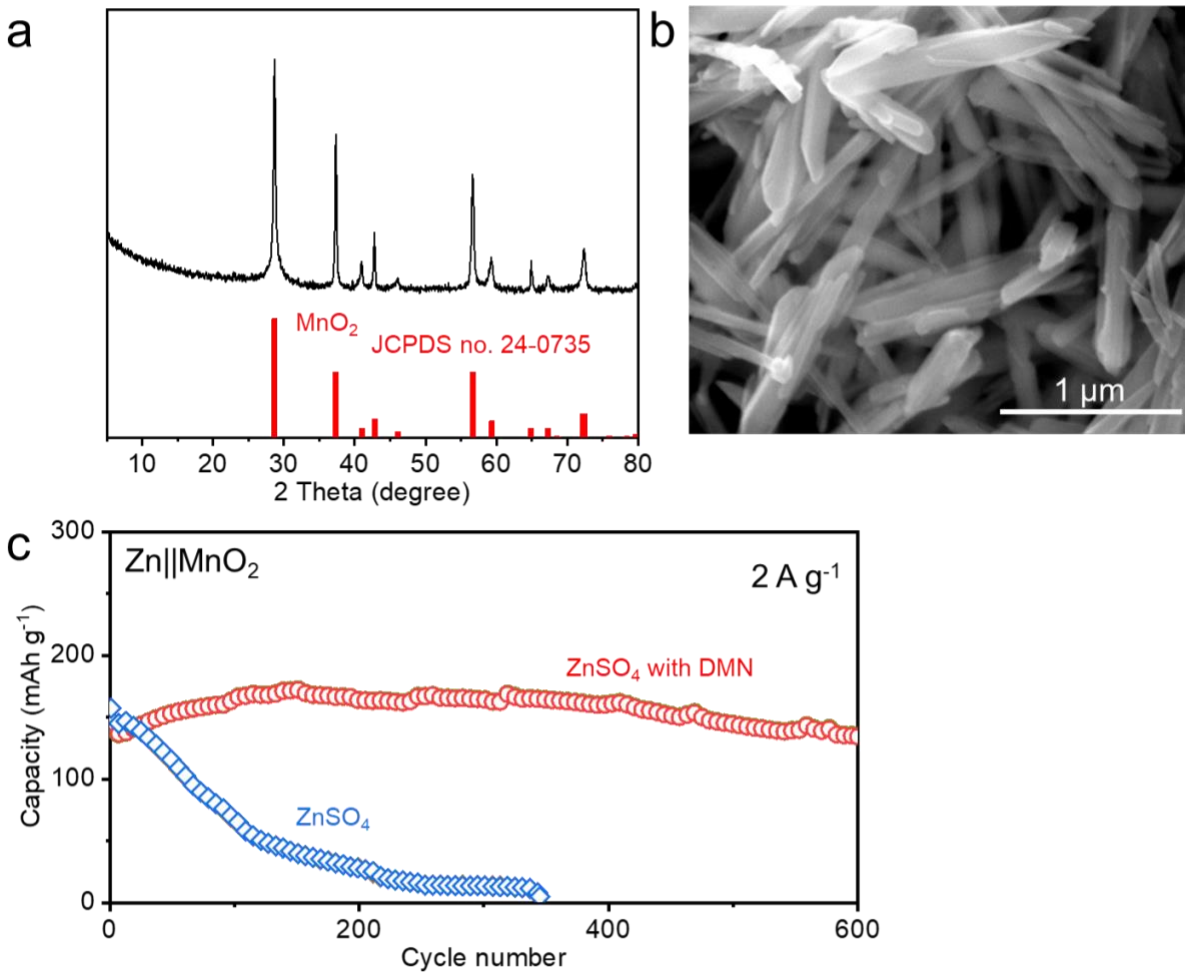

Figure S35. (a) XRD pattern and (b) SEM image of as-prepared MnO_2 powders. (c) The cyclic stability of Zn||MnO_2 full cells at a current density of 2 A g^{-1} under the electrolytes of pure $ZnSO_4$ and $ZnSO_4$ with DMNs.

Table S1. The relative intensity of the cycled electrodes, denoted as I(hkl), is measured in comparison to the intensity of the standard zinc sample, represented as I_0(hkl), which corresponds to JCPDS no.04-003-4142. To obtain accurate results, the background intensity is subtracted from the intensity of cycled electrode. Note that the relative texture coefficients (RTCs) for the {002} crystallographic family comprise both $RTC_{(002)}$ and $RTC_{(004)}$. The relative texture coefficients (RTCs) for each Zn lattice plane are calculated using the following formula:

$$RCT_{(hkl)} = \frac{I(hkl)/I_0(hkl)}{\Sigma\left(I(hkl)/I_0(hkl)\right)} \times 100 \quad \textbf{(S1)}$$

Intensity	002	100	101	102	103	110	004	112	200	201	104
Standard I_0	39.5	23.5	100	14.2	15.3	10	2.3	10.6	1.2	6.5	1.9
With DMN	624773	5496	4279	1001	2197	233	32753	490	174	561	288
Without DMN	6143	2730	15487	4221	5286	946	313	2366	357	1290	680

Movie S1.

The in-situ optical movie records the plating process on the Zn electrode in $ZnSO_4$ with DMNs at 1 mA cm^{-2} . The movie is played in fast forwarded mode at 2 times speed.

Before plating, the Zn electrode is rested for 2 hours in bulk electrolyte (1 mL) containing much more $CuSO_4$ and H_3BTC than in coin cells, which means exccessive generation of DMNs that form aggregates of MOF nanosheets with a size of ~10 μm. These aggregates therefore are large and slow enough to be observed under optical microscope. In the movie, DMNs migrate towards the Zn electrode along the electric potential gradient with the nanosheets parallel to the Zn surface and then disappear after landing on the Zn surface. Note that the majority of nanoscale DMNs, as shown in Figure S5, are too small to be visible under an optical microscope.

References and Notes

1. N. Zhang, F. Cheng, J. Liu, L. Wang, X. Long, X. Liu, F. Li and J. Chen, *Nat. Commun.*, 2017, **8**, 405.
2. H. Jiang, Y. Zhang, Z. Pan, L. Xu, J. Zheng, Z. Gao, T. Hu and C. Meng, *Electrochimica Acta*, 2020, **332**, 135506.
3. O. Yaghi, H. Li and T. Groy, *J. Am. Chem. Soc.*, 1996, **118**, 9096-9101.
4. Y. Fu, G. B. Li, F. H. Liao, M. Xiong and J. H. Lin, *J. Mol. Struct.*, 2011, **1004**, 252-256.
5. Q. Li, A. Chen, D. Wang, Y. Zhao, X. Wang, X. Jin, B. Xiong and C. Zhi, *Nat. Commun.*, 2022, **13**, 3699.